

## REVIEW

[View Article Online](#)  
[View Journal](#) | [View Issue](#)



Cite this: *Mater. Adv.*, 2022, 3, 8081

## An overview on the role of ZnTe as an efficient interface in CdTe thin film solar cells: a review

Deepak Suthar, Sakshi Chuhadiya, Ritika Sharma, Himanshu and M. S. Dhaka \*

The present era of cutting edge technology requires environmentally friendly alternative energy resources due to the limited fuel reserves and the emission of pollutants associated with the use of conventional resources such as fossil fuels. Since the invention of CdTe-based solar cells, they have become potential suitable alternatives and competitors to silicon solar cells owing to their cost effectiveness and stability. Thus, the development of CdTe thin film solar cells has gained significant attention due to their potential roles as sustainable energy sources. To develop higher efficiency CdTe-based thin film solar cell devices, typically, a zinc telluride (ZnTe) layer is employed as an essential interface between the CdTe absorber and metal contact. The superiority of the ZnTe back contact improves the shunting pathway to the motion of charge carriers, which eventually enhances the device performance. With the use of a supporting CdSeTe absorber and magnesium-doped zinc oxide (MZO) optical window together with a ZnTe back contact, these devices are commonly utilized not only in single junction devices but also tandem devices. This review presents major improvements in the power conversion efficiency of CdTe thin film solar cells in detail with special reference to the ZnTe back contact layer. It also highlights various thin film deposition techniques together with the impact of doping and post-deposition treatment on ZnTe thin films to enhance the related properties, followed by the importance of the present study.

Received 11th July 2022,  
Accepted 18th September 2022

DOI: 10.1039/d2ma00817c

[rsc.li/materials-advances](http://rsc.li/materials-advances)

### 1. Introduction and solar cell generations

In the present era, the major challenges include the fulfillment of the increasing energy demand in every sector across the globe including power. Although conventional energy sources such as

coal, oil, and natural gases fulfill the maximum requirement of total energy globally, these resources affect the environment and lifestyle of human beings by emitting pollutants, *e.g.*, the burning of fossil fuels produces greenhouse gases and many hazardous gases, which contribute to global warming. The conventional and non-renewable energy resources have been depleted with time due to their limited availability, and therefore, the search for environmentally clean and safe renewable energy resources should be the focus. Over the past few

*Department of Physics, Mohanlal Sukhadia University, Udaipur-313001, India.  
E-mail: msdhaka75@yahoo.co.in, msdhaka@mlsu.ac.in*



Deepak Suthar

contact-comprised CdTe solar cell devices.

*Deepak Suthar, a PhD scholar at the Department of Physics, Mohanlal Sukhadia University, Udaipur, India, has been a Junior Research Fellow in the Research and Development Project funded by the Department of Science and Technology, Rajasthan, India. He has authored 15 research papers in reputed international journals of high visibility. His research is mainly focused on the growth and characterization of semiconducting materials and ZnTe back*



Sakshi Chuhadiya

*Sakshi Chuhadiya, a PhD scholar at the Department of Physics, Mohanlal Sukhadia University Udaipur, India, is currently Senior Research Fellow awarded by the Council of Scientific and Industrial Research, India. She has authored several papers in reputed international journals of high impact including Coordination Chemistry Reviews. Her current research is mainly focused on the design, synthesis, and applications of metal organic frameworks in solar cell devices.*



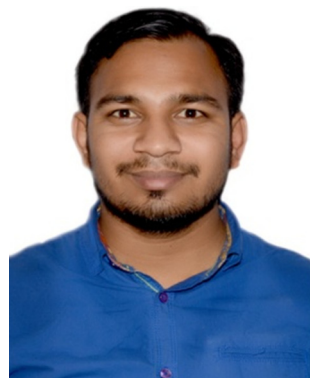
decades, several renewable routes have been considered as cleaner energy sources, which can play a significant role to meet the future energy needs of the society. The excellent use of these resources not only reduces the environmental impact and creates minimum secondary waste but also sustainability, considering the current and future social and economic necessities. The global energy requirement is rising rapidly due to technological advancements together with population explosion, and hence, it is essential to develop reliable, cost-effective, and never-ending renewable energy sources to fulfill the required energy demands arising in the future.<sup>1–8</sup> An overview of the different types of renewable and non-renewable energy resources is pictorially presented in Fig. 1.

Solar energy, among the different types of renewable energy sources such as wind, hydro, tidal, geothermal, and biomass, is a promising and free energy source, with significant potential to address the long-term issues associated with the energy crisis. The sun is a powerful source of solar energy, and the primary forms of solar energy are heat and light. Sunlight is absorbed and transformed by the environment in various ways.



Ritika Sharma

*Ritika Sharma, a PhD scholar at the Department of Physics, Mohanlal Sukhadia University Udaipur, India, is currently a Junior Research Fellow in the Research and Innovation Project funded under RUSA 2.0 Scheme by the Govt. of India and Govt. of Rajasthan. She has authored several research papers in reputed international journals of high visibility such as Solar Energy. Her current research interest includes thin films, CdZnTe and perovskite solar cell devices.*



Himanshu

*Dr Himanshu, a recipient of the INSPIRE Fellowship awarded by the Department of Science and Technology, India, received his PhD from the Mohanlal Sukhadia University Udaipur, India. He has authored more than 40 research papers in reputed international journals of high impact and visibility including AIP conference proceedings and has visited the UAE and UK. His research domain mainly covers thin films and solar cell materials.*

Solar energy has several outstanding features, *e.g.*, it does not have any destructive impact on the ecosystem, is effectively employed for industrial operations, and it is easily affordable, not exhaustible, and provides increasing output in terms of power conversion efficiencies compared to other energy sources.<sup>9–16</sup> The significant features associated with solar energy technology are depicted in Table 1.

Considering the sustainable and abundant availability of solar irradiance on the Earth's surface throughout the year, persistent efforts have been devoted thus far to solar photovoltaic research to develop high-performance and efficient solar cell devices.<sup>17</sup> Solar cell device is a p-n junction diode and works on the principle of the photovoltaic effect, which explains the direct conversion of light into electrical energy.<sup>18</sup> In 1954, the first silicon solar cell was demonstrated at Bell Laboratories, which showed ~6% power conversion efficiency (PCE). Thereafter, continuous research efforts have been made to overcome the complexity in power conversion efficiency and cost effectiveness by demonstrating high-performance devices to meet the energy demands. Solar cell devices are typically categorized into first-, second-, and third-generations based on their development history and absorbers, which are pictorially shown in Fig. 2 and described briefly herein.<sup>19–23</sup> The single/monocrystalline silicon, multi/polycrystalline silicon and GaAs solar cells are considered first-generation solar cells. The second generation comprises thin film-based solar cells, which emerged with low production cost and minimal material consumption. It is noteworthy that the semiconductor materials (especially absorbers) used in the second-generation solar cells have a direct band gap, whereas the first-generation solar cells using silicon material have an indirect band gap. The second generation includes amorphous silicon (a-Si) solar cells, cadmium telluride (CdTe) solar cells, and copper indium gallium diselenide (CIGS) solar cells. The third generation comprises dye-sensitized solar cells (DSSCs), organic solar cells (OSCs), quantum dot solar cells (QDSCs), and perovskite solar cells (PSCs).<sup>19–28</sup>



M. S. Dhaka

*Dr M. S. Dhaka, a recipient of the Raman Postdoctoral Fellowship at Iowa State University, USA, is currently a Professor of Physics at Mohanlal Sukhadia University, Udaipur, India. He supervised four PhDs and has been principal investigator of three research projects funded by UGC, India, DST, Rajasthan and SERB, India. Dr Dhaka has authored more than 100 research papers in reputed international journals of high visibility including AIP and IEEE conference proceedings. His current research mainly focuses on thin films, solar cells, metal organic frameworks and thin film solid oxide fuel cells. He has visited the UK, Norway and USA.*



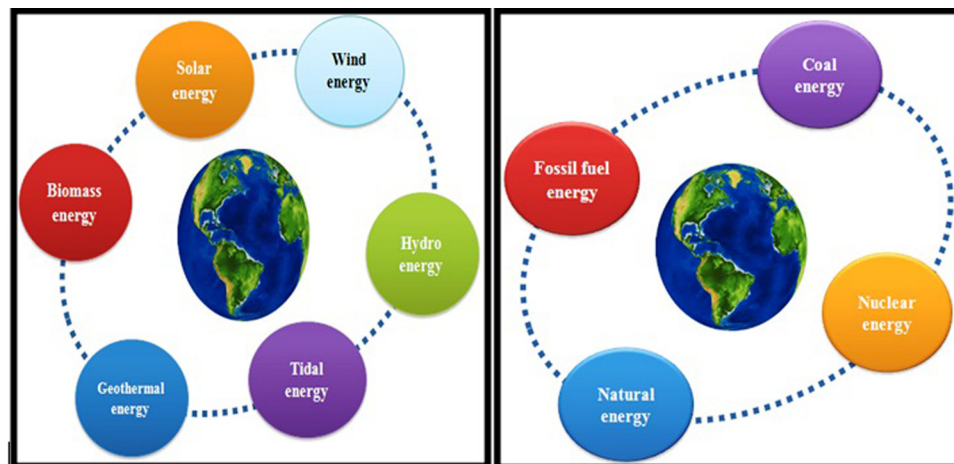


Fig. 1 Pictorial view of renewable and non-renewable energy sources.

A concise explanation of the different solar photovoltaic technologies is presented herein, where the devices are recognized and named according to their absorber layers.

### 1.1 First-generation solar cells

This generation includes silicon wafer-based solar cells, which are also known as conventional or traditional solar cells. As stated, the first silicon-based solar cell was developed in 1954 at Bell Laboratories with a PCE of 6%, and thereafter, substantial research on enhancing the PCE was carried out. First-generation solar cells are of two types: (a) single crystalline silicon solar cells and (b) polycrystalline silicon solar cells.

(a) **Single crystalline silicon solar cells.** These solar cells are also recognized as monocrystalline solar cells and exhibit a high PCE under the standard operating conditions.<sup>29</sup> These solar cells demonstrate higher efficiency, longer life, and better performance compared to others. However, their main drawbacks include high consumption of materials and higher cost compared to the other solar PVs.<sup>30</sup> GaAs-based solar cells are also considered as first generation but they are not prevalent due to the high cost of the germanium substrate, where they are applied owing to lattice matching with the GaAs material.

(b) **Polycrystalline silicon solar cells.** These solar cells are also known as multi-crystalline solar cells. Generally, they are composed of a number of different crystals, which are coupled, and therefore they are also called multi-crystalline solar cells. During the fabrication of these devices, molten silicon is placed

in a graphite mold.<sup>31</sup> The major disadvantage of these solar cells includes their lower power conversion efficiency compared to monocrystalline solar cells.<sup>30</sup>

### 1.2 Second-generation solar cells

These are thin film-based devices having a low production cost and minimal material consumption. As stated, there are three types of solar cells in this generation, as follows: (a) amorphous silicon (a-Si) solar cells, (b) cadmium telluride (CdTe) solar cells, and (c) copper indium gallium diselenide ( $\text{CuIn}_x\text{Ga}_{1-x}\text{Se}_2$ , *i.e.*, CIGS) solar cells.

(a) **Amorphous silicon solar cells.** In amorphous silicon solar cells, a thin layer of an order of micron is used as an absorber layer. They possess a maximum PCE of ~14% at the laboratory scale,<sup>32</sup> dominating the market but less expensive compared to the crystalline silicon devices. These solar cells have the advantage of low manufacturing cost, great potential, large-scale production, and light weight, but possess some disadvantages including lower efficiency to incident photon absorption compared to crystalline silicon solar cells and degradation of the material, causing instability in the related devices.<sup>33</sup>

(b) **Cadmium telluride solar cells.** In this technology, cadmium telluride (CdTe) thin film with a thickness of 3–5  $\mu\text{m}$  is used as an absorber layer. CdTe-based solar cells have shown maximum PCE of 22.1% at the laboratory scale by incorporating the graded absorber CdSeTe.<sup>32</sup> CdTe photovoltaic technology has

Table 1 An overview of the significant features associated with solar energy technology

Significant feature(s)	Comment(s)
Eco-friendly nature	Unlike conventional power sources, solar system produces no harmful emissions to the environment.
Silent	Solar panels do not make any noise during the process of converting sunlight into electricity.
Durability	Solar panels do not contain any movable parts, and therefore, the probability of them being damaged is very low.
Cost effectiveness	Solar energy is more cost effective compared to other energy sources based on several aspects.
Solid home investment	Solar energy saves money and the investment made on solar panels add value to the home.
Ahead of the curve	The future of the world would be renewable and clean energy driven. The conversion of solar energy into electricity would be a step ahead to meet the energy need of society.
Low-maintenance	Once solar panels have been installed and their efficiency is maximized, and subsequently they require very little maintenance, although each technology has a certain lifetime.



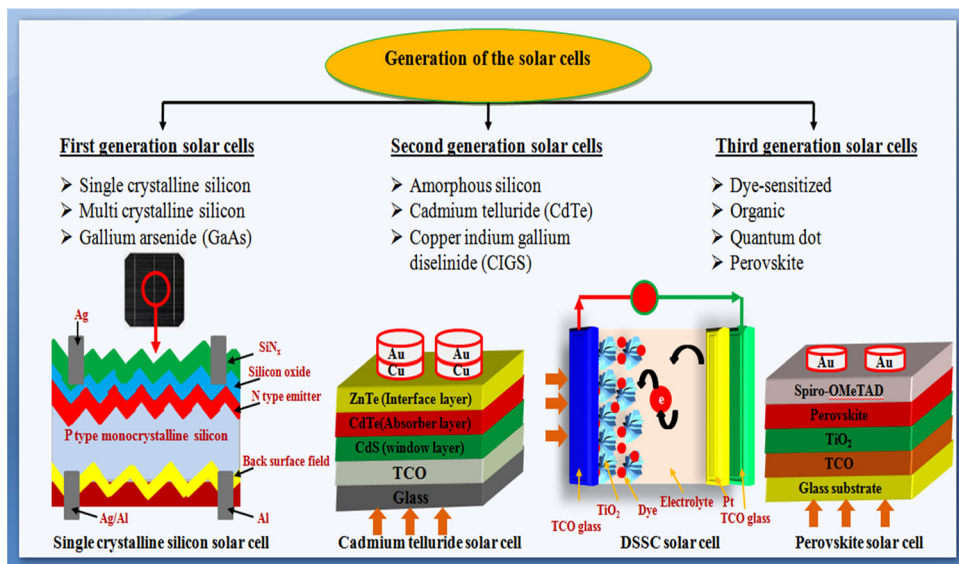


Fig. 2 Classification of solar cells based on their generation.

attracted attention potentially due to its thermal and chemical stability. It is suitable for utility-scale applications to reduce the cost of electricity per watt.<sup>34</sup>

#### (c) Copper indium gallium diselenide (CIGS) solar cells.

CIGS solar cells are made from a thin layer of direct band gap semiconducting material of copper indium gallium diselenide Cu<sub>(In,Ga)Se<sub>2</sub></sub>. CIGS cells have shown an efficiency of up to 23.3%, having similar durability to that of silicon solar cells.<sup>32,35</sup>

### 1.3 Third-generation solar cells

The high production cost of first-generation solar cells and the limited availability of materials for second-generation solar cells have invited a new generation, which emerged and recognized as the third generation of solar cells. Third-generation solar cells are naturally different from the earlier explained first and second generations including device design evolution and interface engineering. The third generation comprises several solar cell classes, which are also explained herein.

(a) **Dye-sensitized solar cells (DSSCs).** DSSCs are comprised of a working electrode, dye-sensitizer, redox-mediator (electrolyte), and counter electrode. Typically, they are constructed by employing two conductive transparent materials, which act like current collectors and have two main characteristics, *i.e.*, high transparency of >80% to permit the maximum incident irradiance towards the effective area of the device and high electrical conductivity for efficient charge transfer with reduced energy loss. Although TiO<sub>2</sub> thin layers are typically applied as the working electrode in DSSCs due to their high band gap, non-toxicity, cost effectiveness and easy availability, they only absorb a small amount of light in the UV region, which can be mitigated by encapsulating them in a mixture of photosensitive molecular sensitizer and a solvent. The soaking in dye solution results in the attachment of a large number of dye molecules on the nanocrystalline TiO<sub>2</sub> surface owing to its

high porosity and large surface area, and then the light absorption increases on the surface. The recorded power conversion efficiency for these devices is 13% on the laboratory scale.<sup>32,36</sup>

(b) **Organic solar cells.** Organic solar cells were developed by organic polymers to absorb light, and the manufacturing cost of an organic solar cell is low due to the use of inexpensive precursors. Remarkable progress has been recorded in the very short history of organic solar cells by attaining a laboratory efficiency of more than 18%.<sup>32</sup> In these solar cells, one of the electrodes must be transparent to enable it to also act as a window to incident light. However, the main drawbacks of organic solar cells are their lower efficiency, stability and strength compared to the champion silicon solar cells.<sup>37</sup>

(c) **Quantum dot solar cells.** In these solar cells, quantum dots are used as the absorber to absorb incident irradiance. Quantum dots are a special category of semiconductors, which can confine electrons to where the band gap of the quantum dots can be tuned by size evolution. To date, quantum dot-based solar cells have attained a power conversion efficiency of 18.1%<sup>32</sup> and attracted attention from researchers due to their adaptable properties, cost effectiveness and lightweight or portability.<sup>38</sup>

(d) **Perovskite solar cells.** In 2009, Miyasca's group, incorporated an organic inorganic hybrid lead halide perovskite, methyl ammonium lead iodide (CH<sub>3</sub>NH<sub>3</sub>PbI<sub>3</sub> or MAPbI<sub>3</sub>), in a liquid-electrolyte-based dye-sensitized solar cell (DSSC), which is recognized as a perovskite solar cell (PSC), with the PCE of this type of device increasing from 3.1% to 25.7% up to 2022, which is now rivaling the champion silicon devices in few aspects.<sup>32</sup> The perovskite solar cells (PSCs) consist of a perovskite-structured (ABX<sub>3</sub>) material as the active/absorber layer. This is a very attractive alternative for commercial applications because this type of cell is very cheap to scale up the process. Perovskite solar cells have emerged as the most outstanding solar cells in terms of efficiency, and therefore researchers have devoted tremendous attention to perovskite solar cells.



These solar cells exhibit some advantages including flexibility and lightweight.<sup>39,40</sup>

Each generation of solar cells has certain merits and drawbacks and the performance of the device is affected by the properties of their constituents and growth conditions.

Among the different types of solar cells, thin film solar cell technology has gained huge attention due to its incredibly controlled production costs through the reduced consumption of constituent layer materials by optimizing the thickness and other conditions. Thin film solar cells are promising devices for global photovoltaics due to their wide diversity of choices in terms of device fabrication and design. In the fabrication of thin film solar cells, various types of substrates can be applied in accordance with the device architecture. To develop constituent layers, *i.e.*, absorber, window/buffer and interface layers, a variety of strategies has been developed, which can be categorized as physical and chemical routes, which have their own merits and disadvantages. The deposition techniques and conditions allow tailoring and engineering the properties of the different constituent layers of solar cells to improve the device performance. A true understanding and knowledge of the thin film deposition processes can assist in achieving high

performances. The growth and characterization to fabricate the constituent layers with simple manufacturing processes need to be studied.<sup>41–46</sup> Among the second-generation solar cells, for the development of CdTe thin film solar cell devices, the typical architecture used thus far is glass/TCO/CdS/CdTe/ZnTe/metal contact, while in recent years, due to the evolution of materials, modified architecture as Glass/MZO/CdSeTe/CdTe/ZnTe/metal contact has also been applied to achieve an elevated performance, where MZO (magnesium-doped zinc oxide) is used as a window layer instead of the conventional CdS together with CdSeTe ( $\text{CdSe}_x\text{Te}_{1-x}$ )/CdTe as a graded absorber. An illustration of the typical CdSeTe/CdTe architecture device is provided in Fig. 3 together with its energy band diagram and the features of thin film solar cells.

CdTe solar cells are widely used because CdTe is an emerging material with unique properties such as direct optical energy band gap (1.45 eV), high chemical stability, and large absorption coefficient.<sup>47–54</sup> In CdTe-based thin film solar cells, mismatching of the CdTe valence band level and electrode metal work function results in open circuit voltage loss, and thus the desired efficiency cannot be achieved. To enable facile hole transportation, ZnTe is employed as a back contact interface, which also

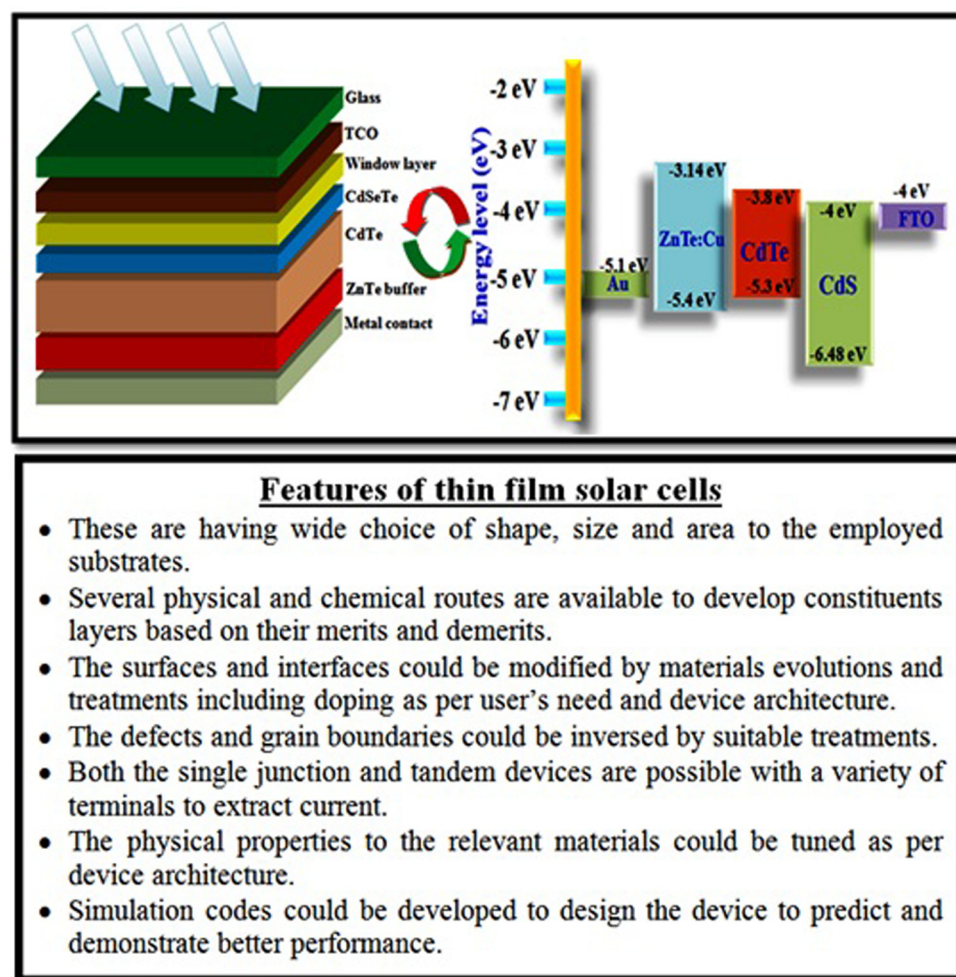


Fig. 3 Pictorial view of the CdSeTe/CdTe solar cell device architecture, typical energy band diagram and features of thin film solar cells.



resolves issue of the presence of a Schottky barrier due to the high electron affinity and lower charge carrier concentration of the CdTe material.

Traditionally, a CdS window layer is employed to develop CdTe solar cells, where during the CdTe deposition and CdCl<sub>2</sub> treatment, interdiffusion happens at the CdS/CdTe interface, and consequently CdS<sub>1-y</sub>Te<sub>y</sub> is alloyed in the window layers and CdTe<sub>1-x</sub>S<sub>x</sub> in the CdTe absorber, where CdS<sub>1-y</sub>Te<sub>y</sub> is not only highly defective but photo-inactive<sup>55</sup> too and the CdTe<sub>1-x</sub>S<sub>x</sub> alloy reduces band gap. The diffusion of S into CdTe enhances the photocurrent collection in longer wavelength regions (825–865 nm). Although to obtain a suitable band gap, a significant amount of S should be incorporated in CdTe but the solubility of CdS in CdTe is established to be very low due to the large size mismatch between S and Te.<sup>56,57</sup> Se has lower size mismatch with Te than S, and consequently CdSe has greater solubility in CdTe compared to CdS.<sup>55</sup> The band gap in the CdTe<sub>1-x</sub>Se<sub>x</sub> alloy is reduced from 1.4 eV to 1.32 eV and the photocurrent is improved, which eventually leads to an increment in power conversion efficiency.<sup>58</sup> The recombination loss associated with the back surface of CdTe devices can also be reduced by inserting the wider band gap ZnTe as the back contact layer between the absorber and metal contact, and compliance work demonstrated a power conversion efficiency of ~20%.<sup>59</sup>

To improve the performance to CdTe-based solar cells, in recent years, researchers have mainly focused on two features including replacement of the traditional CdS window layer by a wide band gap and fully transparent material such as Zn<sub>1-x</sub>Mg<sub>x</sub>O (ZMO)<sup>60–63</sup> for advancement in photocurrent and the introduction of Se in CdTe to form a graded band gap CdSeTe/CdTe absorber, which can passivate the front surface to increase the carrier lifetime and absorption in the longer wavelength region simultaneously.<sup>64</sup> An efficiency of ~16% was reported by Samoilenko *et al.*<sup>65,66</sup> by using a magnesium-doped zinc oxide (MZO) window layer in CdTe solar cells. The introduction of Se in the form of a CdSeTe layer at the interface with magnesium-doped zinc oxide (MZO) resulted in a

PCE of 18.6%<sup>61</sup> and ~19%<sup>67</sup> under similar conditions. Metzger *et al.*<sup>68</sup> predicted a PCE of ~20.8% by employing simulation modeling for a graded CdSeTe/CdTe absorber layer doped with arsenic (As). The recorded efficiency of 22.1% was attained by applying the architecture of glass/FTO/MZO/CdSeTe/CdTe/ZnTe/metal contact.<sup>69,70</sup> However, further work is required to get improved the PCE of CdTe-based solar cells.

Considering the above, ZnTe is an important and environmentally friendly material, belonging to II–VI group compound semiconductors and having a wide direct band gap (2.26 eV) and low electron affinity (3.53 eV),<sup>71–81</sup> which is suitable to increase the PCE of CdTe solar cell devices. An overview of the properties together with deposition and characterization techniques for the ZnTe thin film layers is shown in Fig. 4, which can be considered for the development of the layers and devices.

A pictorial view of the unit cell of ZnTe is depicted in Fig. 5 together with the architecture of the recently developed high-performance device, where the traditional CdS layer is replaced by an eco-friendly and better optical window, *i.e.*, magnesium-doped zinc oxide (MZO).

Considering the current societal energy needs and device development challenges, in the present review, we explore the potential role of the ZnTe material as an efficient interface for CdTe thin-film solar cells by means of their different properties and applications in solar cells together with the relevant deposition techniques. This review is organized into the main deposition techniques used thus far, followed by an emphasis on the properties of ZnTe single layers, their potential role in device design and development with further road map to resolve challenges.

## 2. Deposition techniques

Thin film solar cells are comprised of several thin film layers and a variety of strategies is available thus far to develop them,

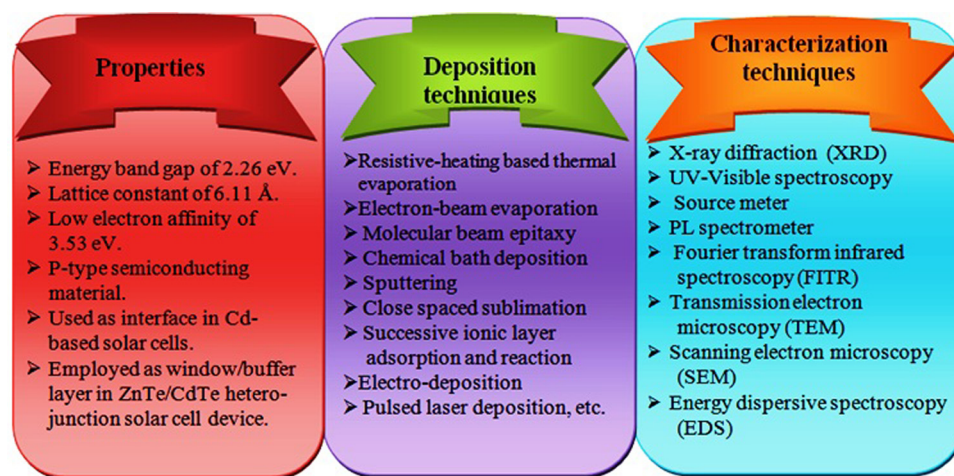


Fig. 4 Overview of the properties, deposition and characterization techniques for ZnTe thin layers, which can be considered during material evolution and device development.



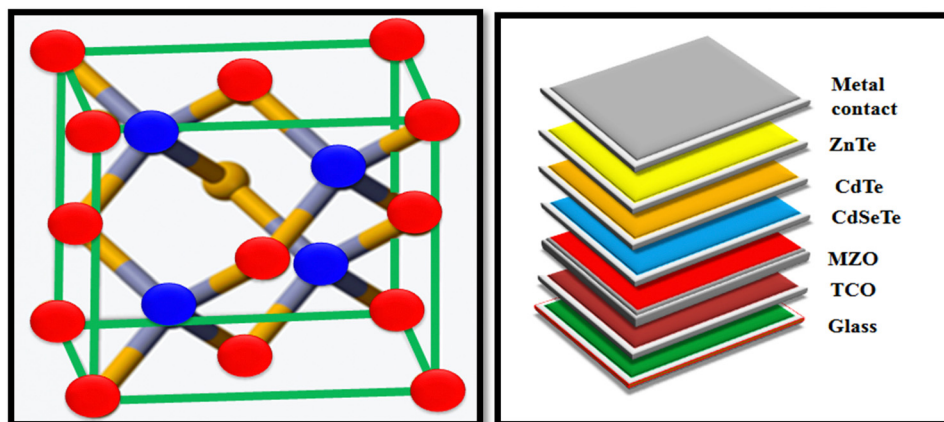


Fig. 5 Pictorial view of the unit cell of the ZnTe and device architecture comprised of ZnTe as the back contact, where the CdS optical window is replaced by an MZO layer.<sup>65,66</sup>

where transparent conducting oxides such as indium-doped tin oxide (ITO) and fluorine-doped tin oxide (FTO)-coated glasses are used as the substrates in the superstrate device architecture and the resistive heating-based thermal evaporation technique is typically employed for the formation of the metal contact. Thin film solar cells can be developed with better efficiency and stability by optimizing the thickness and properties of their different constituent layers, *i.e.*, window, absorber, buffer and contact layers. As stated, a variety of deposition techniques has been employed thus far to grow the constituent layers, which are classified as follows: (a) physical and (b) chemical routes, where the resistive heating thermal evaporation, electron beam

evaporation, molecular beam epitaxy, sputtering, and electro-deposition techniques have been used thus far for the fabrication of ZnTe thin films,<sup>82–97</sup> providing diverse properties. An overview of the physical and chemical routes is presented in Fig. 6, and considering their merits and drawbacks, the major deposition techniques are discussed in following section.

## 2.1 Resistive heating thermal evaporation technique

Over the years, the resistive heating thermal evaporation technique has been the most commonly used method to deposit ZnTe thin films, which is a simple, low cost, reproducible and excellent technique with optimum control over the deposition rate,

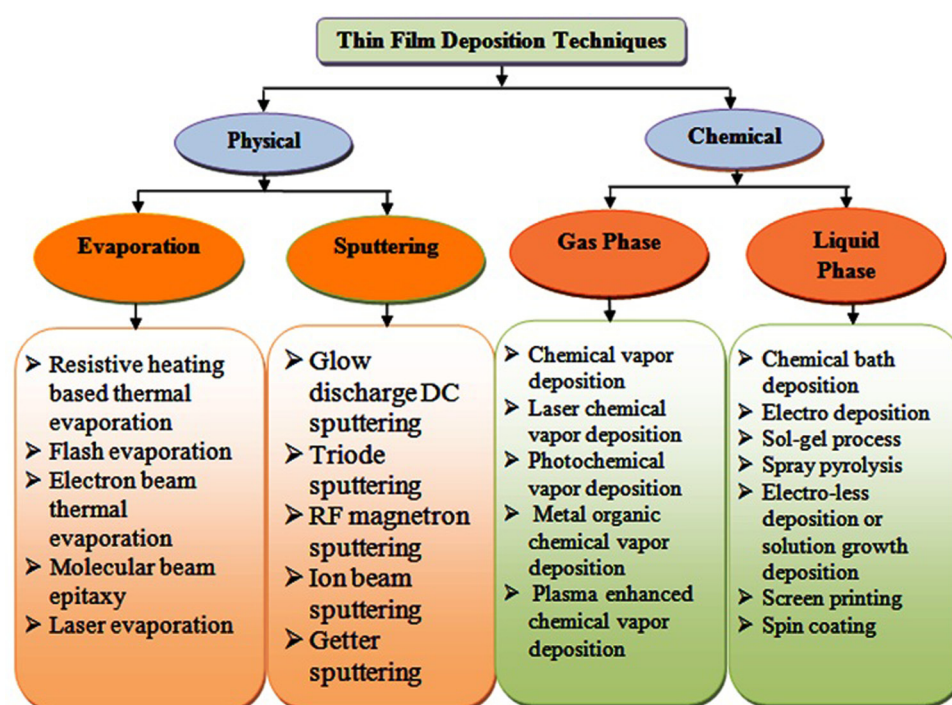


Fig. 6 Classification of thin film deposition techniques.<sup>98</sup>



substrate temperature, and film thickness.<sup>84,99–104</sup> Numerous researchers have employed this technique to fabricate ZnTe thin films and solar cell devices.<sup>105–109</sup> In the thermal evaporation technique, the source material is kept in a filament (boat of molybdenum, tungsten, and tantalum or tungsten basket), where the source material is heated to its melting point using electrical energy under high vacuum. A higher vacuum is required to enhance mean free path of the evaporants to minimize the contamination during the deposition due to existence of residual gases. The film growth process involves nucleation, coalescence, channels, holes, and continuous film deposition.<sup>110,111</sup> A pictorial view of the resistive heating thermal evaporation technique together with its advantages and disadvantages is depicted in Fig. 7.

Using the resistive heating thermal evaporation technique, ZnTe thin films having a thickness 300 nm were deposited on glass substrates at room temperature with vacuum of  $10^{-6}$  Torr and the findings showed that it is suitable for photodetector applications.<sup>112</sup> The impact of Cu doping on the physical properties of ZnTe thin films were investigated employing the thermal evaporation technique in the vacuum range of  $\sim 3 \times 10^{-4}$ – $10^{-7}$  torr, where the conductivity was varied, demonstrating DC conductive behavior and translational hopping motion at low and high frequency, respectively.<sup>99</sup> The elemental composition also affects the properties, and accordingly stoichiometry changes were investigated for thermally evaporated 2500 nm ZnTe thin films grown at the substrate temperatures of  $-123$  °C and  $27$  °C.<sup>113</sup> The thermal evaporation technique was used to grow films with a thickness of 85 nm, 300 nm, 600 nm, and 900 nm on silicon and glass substrates<sup>114–117</sup> and thickness of 200 nm, 400 nm, 600 nm, and 1000 nm at the growth temperature  $300$  °C for optoelectronic applications.<sup>118</sup> Indium-doped ZnTe films were fabricated on glass substrates at vacuum of  $10^{-5}$  Torr and the findings demonstrated the enhanced conductivity of the doped films.<sup>119</sup> ZnTe- and Ga-doped ZnTe thin films were fabricated on glass and Te-doped GaSb substrates at vacuum of  $10^{-5}$  mbar.<sup>120</sup> Similarly, Cu- and

Ag-doped ZnTe thin films were deposited on glass substrates at  $7.5 \times 10^{-5}$  Torr.<sup>121</sup> The ZnTe films were deposited on tantalum and single-crystal silicon substrates at angles of  $0^\circ$ ,  $20^\circ$ ,  $40^\circ$ ,  $60^\circ$ , and  $80^\circ$ , where the results demonstrated their potential for solar cell, detector, and transistor applications.<sup>122</sup> Cu-doped ZnTe films were developed for photovoltaic applications employing this technique, where doping was undertaken by the melt growth technique.<sup>123</sup> The films grown by the thermal evaporation technique demonstrated good uniformity and quality, and thus this method can be widely used for the formation of contacts in all types of devices including solar cells and sensors. Pristine films could be subjected to local thermal treatment inside the deposition chamber to get better-quality films<sup>124–126</sup> in accordance with the device architecture. The parameters obtained thus far employing this method are depicted in Table 2.

In the deposition of several materials including oxides and due to the radiant heat effect, alternative methods are needed to achieve thermal evaporation, which is bridged by the electron beam evaporation method in a few aspects and discussed in the following section.

## 2.2 Electron beam evaporation technique

In the electron beam evaporation technique, an electron beam is used to irradiate the source material under high-vacuum conditions. The source material is kept in a graphite crucible and bombarded by an accelerated electron beam in the typical voltage range of 5–20 kV. Electron beam bombardment results in the evaporation of the source material, and subsequently the evaporants move towards the substrates followed by thin film growth *via* the prevalent growth mechanism. An overview of the typical electron-beam experimental setup together with its advantage and disadvantage is comprised in Fig. 8.

The electron beam evaporation technique is widely used due to its advantages including development of high-quality uniform thin films with repeatable accuracy, good stoichiometry and purity. To develop cost-effective layers, 400 nm thin ZnTe films

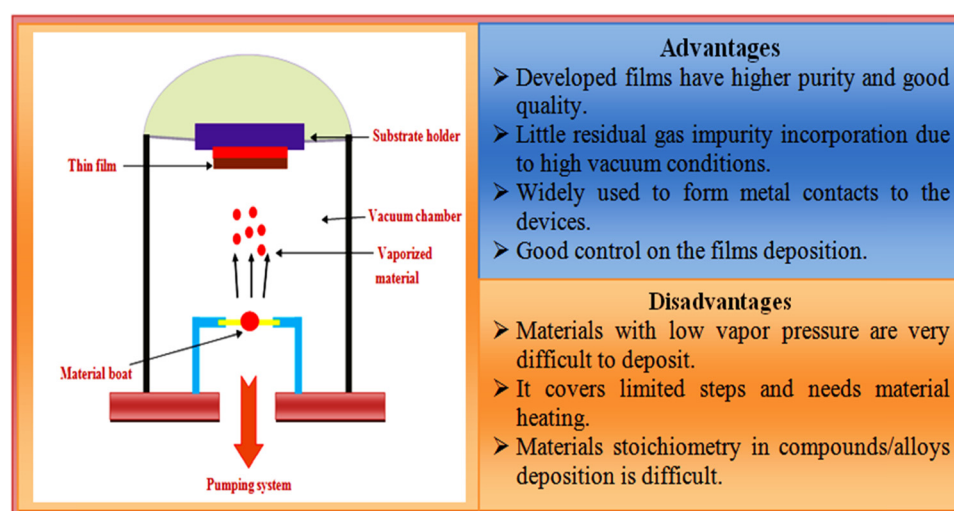


Fig. 7 Overview of the resistive heating thermal evaporation technique together with the advantages and disadvantages of this method.



Table 2 The ZnTe film parameters obtained by resistive heating thermal evaporation deposition method

S. no.	Vacuum level (torr)	ST/AT (°C)	$E_g$ (eV)	$D$ (nm)	$\rho$ (Ω cm)	$E, \mu, R_o/R_i$	Ref.
1	$3.0 \times 10^{-6}$	R.T. 100 200 300	2.31 2.10 2.37 2.74	22 29 39 42	—	—	123
2	$2.2 \times 10^{-5}$	25	—	—	—	$\varepsilon = 8.19$ , cubic phase	110
3	$7.5 \times 10^{-6}$	25	—	50–80	$2.5 \times 10^4$ – $1.7 \times 10^7$	Cubic phase and ohmic nature	111
4	$10^{-6}$	25	2.20	4–5	—	—	112
5	$2.2 \times 10^{-4}$	–123	2.13	46	32	Cubic phase	113
6	$10^{-5}$	27 100 200 280	2.16 — — 2.26	52 43 50 55	$1.0 \times 10^4$ 1538 709 310 287	$\mu = 12.8, R_o/R_i = 3.73$ $\mu = 21.2, R_o/R_i = 5.23$ $\mu = 36.9, R_o/R_i = 15.33$ $\mu = 37.6, R_o/R_i = 21.11$	188

Where ST: substrate temperature, AT: annealing temperature,  $E_g$ : optical energy band gap,  $\rho$ : resistivity,  $\mu$ : mobility, and  $R_o/R_i$ : output and input resistance ratio.

were deposited by electron beam evaporation at the base vacuum of  $1.5 \times 10^{-6}$  Torr, which showed high quality and promising results.<sup>127</sup> As stated, doping also alters the film quality and device performance, and accordingly vanadium-doped and undoped ZnTe thin film were prepared using the e-beam technique under vacuum of  $\sim 8 \times 10^{-6}$  Torr to explore impact of temperature on electrical properties.<sup>128</sup> Electron beam-evaporated ZnTe thin films were used in photodiode sensor devices as a buffer layer with the architecture of p-ZnTe:N/CdTe:Mg/n-CdTe:I/GaAs.<sup>129</sup> Employing this technique, ZnTe films were developed with a thickness of 200 nm and 300 nm at the base vacuum of  $\sim 7.5 \times 10^{-6}$  Torr as interface layers,<sup>82</sup> thickness of 100 nm,<sup>84</sup> 300 nm<sup>130</sup> and in the range of 100–500 nm<sup>131</sup> at vacuum of  $7.5 \times 10^{-6}$  Torr as the back contact layers. The obtained film parameters employing this method are presented in Table 3 with the corresponding references.

However, despite its numerous merits, the electron beam technique suffers from the disadvantage of high vapour pressures depending on the source materials and ensuring the stoichiometry is also a challenging task. Thus to overcome these

challenges, more specific technique such as molecular beam epitaxy can be employed, which offers the advantages of high purity and oxide-free deposition. According to these perspectives, in the next section, we present the molecular beam epitaxy (MBE) technique together with its role in device development.

### 2.3 Molecular beam epitaxy (MBE) technique

Molecular beam epitaxy (MBE) is the cleanest and most demanding technique utilized to grow thin films, which is performed under ultra-high vacuum (UHV) conditions and widely used to maintain the stoichiometry thus far. A pictorial view of the typical experimental setup together with its advantages and disadvantages is shown in Fig. 9. It consists of two or more Knudsen effusion cells (K-cells), located at bottom of a UHV chamber and aligned towards the center of the chamber, where the sample holder with substrates is positioned. Each K-cell is comprised of individual elements of interest in ultra-pure solid form, from which the desired film development occurs. The growth process is started by heating the K-cells corresponding to their melting point temperatures until the elements in each cell vapourise,

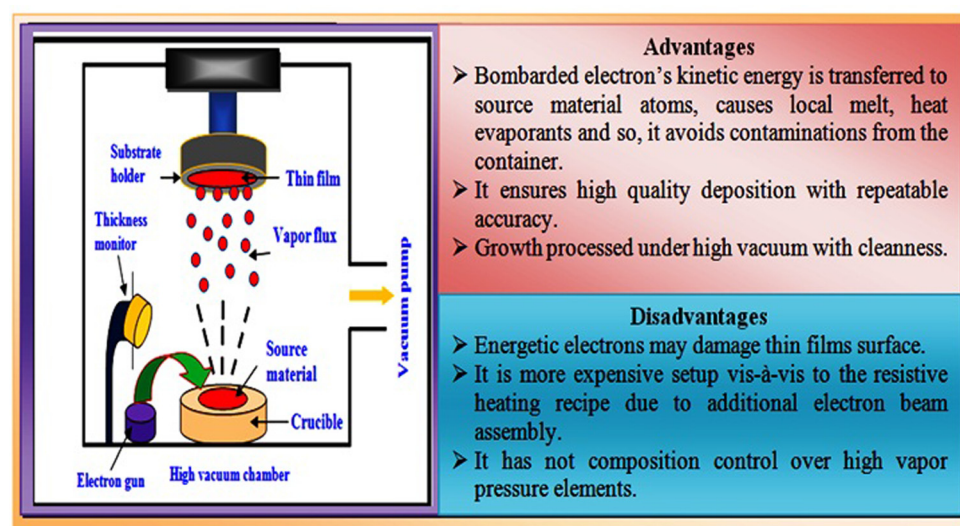


Fig. 8 Overview of electron beam evaporation technique together with the advantages and disadvantages of this method.



Table 3 The film parameters obtained by e-beam evaporation technique

S. no.	Vacuum level (torr)	DR ( $\text{\AA s}^{-1}$ )	$E_g$ (eV), $n$	$D$ (nm)	Phase and other(s)	Ref.
1	$7.5 \times 10^{-6}$	8.5	$E_g = 2.58\text{--}2.76$	23 $\text{--}$ 52	Cubic	181
2	$6 \times 10^{-7}$	8	$E_g = 2.265$ $n = 2.548$	26	Cubic, $\varepsilon = 8.6 \times 10^{-3} \text{ lin}^{-2} \text{ m}^{-4}$	193
3	$6 \times 10^{-6}$	2.05	—	—	Amorphous, P-type	128
4	$2.2 \times 10^{-4}$	3	$E_g = 2.23$	46 $\text{--}$ 52	Cubic	113
5	$10^{-5}$	—	$E_g = 2.26$	38 $\text{--}$ 52	Cubic	28
6	$1.50 \times 10^{-6}$	4	$E_g = 2.24$	$\sim 60$	Cubic	127

Where DR: deposition rate,  $n$ : refractive index, and  $\varepsilon$ : relative permittivity.

following by reaching the substrates fixed at the holder, where the evaporants are deposited in accordance with the prevalent film growth mechanism, as stated earlier, and to achieve uniform growth, the substrates are continuously rotated at low rotation speeds with help of a stepper motor embedded with a magnetic manipulator.

Thus, considering its merits, nitrogen-doped ZnTe thin films were developed employing the molecular beam epitaxy method by obtaining significant grain growth,<sup>132</sup> and for their application in detectors and optoelectronic devices, the films were grown on GaAs substrates with better crystallinity.<sup>133</sup> However, despite these merits, to employ this technique in deposition of thin films and devices associated with high crystallinity, it requires a longer processing time together with high vacuum compared to other techniques, and thus new options are necessary with certain merits. The following section presents the sputtering technique.

#### 2.4 Sputtering deposition technique

Sputtering is a physical vapor deposition (PVD) technique and a physical route, which is classified based on the applied power source mainly as dc and rf sputtering, where the former uses a dc power supply, whereas the latter employs an rf supply with impedance matching. In this method, thin film deposition is undertaken by a speed transfer process, where the atoms or

molecules of the desired material are expelled from a target through bombardment of high energy particles. Sputtered atoms are ejected from the target with a wide range of energies. The ejected atoms move towards the substrates, followed by condensation, and then high-quality thin film deposition in accordance with the merits of this technique. The experimental setup together with the advantages and disadvantages of the sputtering technique is shown in Fig. 10.

Considering the advantages of the sputtering technique, ZnTe thin films were developed employing this method and the films exhibited high uniformity and homogeneity.<sup>134</sup> For their application as a digital image filter,  $\sim 2.4 \mu\text{m}$  films were deposited on GaSb and InAs substrates at the substrate temperature of  $330^\circ\text{C}$ .<sup>135</sup> For optoelectronic devices, 250 nm films were developed at different substrate temperatures using rf magnetron sputtering with a base vacuum of  $1.1\text{--}1.2 \times 10^{-2}$  Torr.<sup>136</sup> On applying sputtered ZnTe films as the back contact of CdTe solar cells, the devices demonstrated a significant improvement in stability and performance.<sup>137</sup> These films were also deposited on a glass substrate with 50 W RF power and  $\sim 1.5 \times 10^{-6}$  Torr base vacuum.<sup>138</sup> To develop intermediate band semiconductors, ZnTe:O films were deposited using this technique.<sup>139</sup> The ZnTe:Cu thin films prepared were applied as back contacts in CdS/CdTe devices.<sup>140</sup> The obtained relevant parameters for cubic-phase films using this technique are depicted in Table 4.

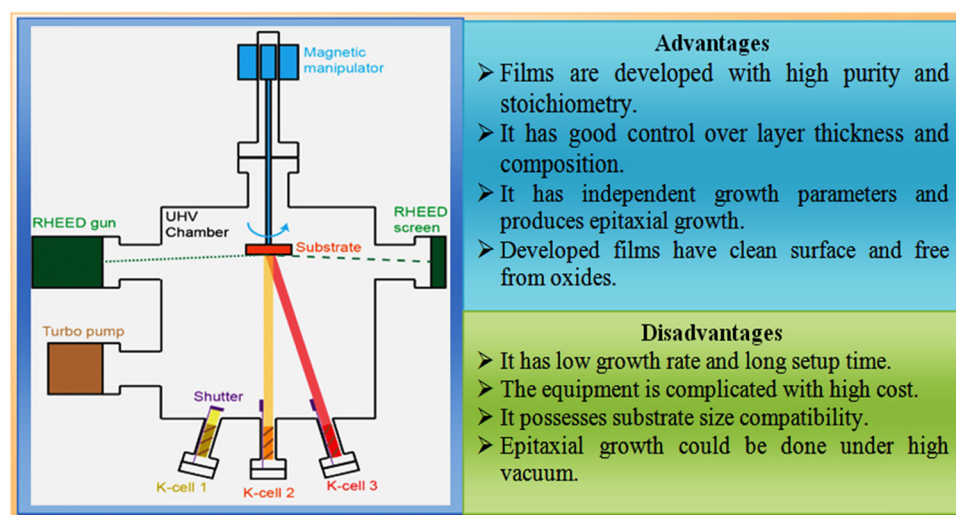


Fig. 9 Overview of molecular beam epitaxy experimental setup together with its advantages and disadvantages.



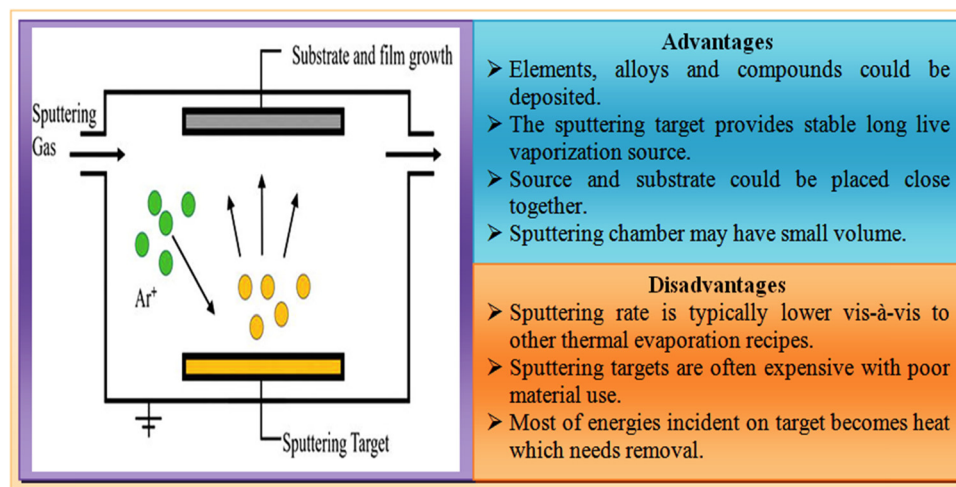


Fig. 10 Pictorial view of the sputtering technique together with its advantages and disadvantages.

However, the high cost of sputtering targets is the major drawback of this technique, which requires alternatives.

## 2.5 Electrodeposition technique

The electrodeposition method is a chemical route-based technique applied for the uniform coating of substrates or electrodes with a controlled film thickness, where electrochemical redox reactions occur on passing a current through an electrochemical cell comprised of the precursors of interest.<sup>141</sup> This technique requires a low investment and enables production on a large scale with some limitations regarding the shape and size of the materials of interest.<sup>112</sup> An outline of the electrodeposition experiment together with its advantages and disadvantages is shown in Fig. 11.

Considering the merits and disadvantages of the electrodeposition technique, ZnTe films were grown on conductive oxide substrates for application in photoelectrochemical devices,<sup>142</sup> optimized for electronic devices<sup>143</sup> and evolved based on the electrodeposition temperature on FTO-coated glass substrates as the window layer in solar cell devices.<sup>144</sup> For their application as a hetero-partner in solar cells, films were prepared followed by chloride activation with the architecture of glass/FTO/n-CdS/p-ZnTe/Au.<sup>145</sup> Cu-doped and undoped ZnTe films were developed on metal substrates using this technique, where the obtained electrical properties were altered by the incorporation of a dopant.<sup>146</sup>

Considering the required technology, these films have also been developed thus far by employing laser evaporation, ion beam sputtering, laser chemical vapor deposition, plasma enhancement, chemical bath deposition, spray pyrolysis, liquid

phase screen printing, pulsed laser deposition, spin coating and sol-gel techniques.<sup>147–156</sup> The obtained film parameters are presented in Table 5 for electrodeposition together with the other chemical and physical route-based techniques such as SILAR, PLD and CSS.

Persistent efforts have been devoted thus far to insert ZnTe films as constituent layers to develop high-performance devices employing a variety of techniques, as detailed above, which are associated with some merits and drawbacks. Accordingly, resistive heating-based thermal evaporation is a widely used technique owing to its simplicity, easy operation, optimum material utilization, high purity thin film deposition and controlled deposition rate together with its availability in most laboratories across the globe given that it is mandatory for metal contact formation to the device. As stated, the film properties are also altered by doping with a suitable dopant to satisfy the device need. The developed thin film layers need to be optimized for the associated technology, which can be undertaken using the corresponding characterization tools. Thus, a brief outline of the doping and characterization is included in the following sections.

## 3. Impact of doping and post treatment on physical properties

The ZnTe is a p-type semiconducting material belonging to the II–VI group, which has attracted significant attention from the solar cell community due to its outstanding physical properties

Table 4 Parameters of cubic phase ZnTe films employing the sputtering deposition technique

S. no.	Vacuum level (torr)	Ref. gas	Optical parameters		Electrical parameter			Phase	Ref.
			$E_g$ (eV)	n	D (nm)	$\rho$ ( $\Omega$ cm)	$E_a$ (eV)		
1	$8.9 \times 10^{-5}$	Ar	2.26	2.55	13	—	0.48	Cubic	93
2	$1.2 \times 10^{-2}$	N	2.13–2.20	—	3–19	$1.4 \times 10^4$ –1.5	—	Cubic	136
3	$9.9 \times 10^{-4}$	Ar	—	—	—	—	—	Cubic	137
4	$1.33 \times 10^{-5}$	Ar	2.31–2.26	—	27–50	—	—	Cubic	189
5	$3 \times 10^{-6}$	Ar	2.3–2.6	—	—	—	—	Cubic	139



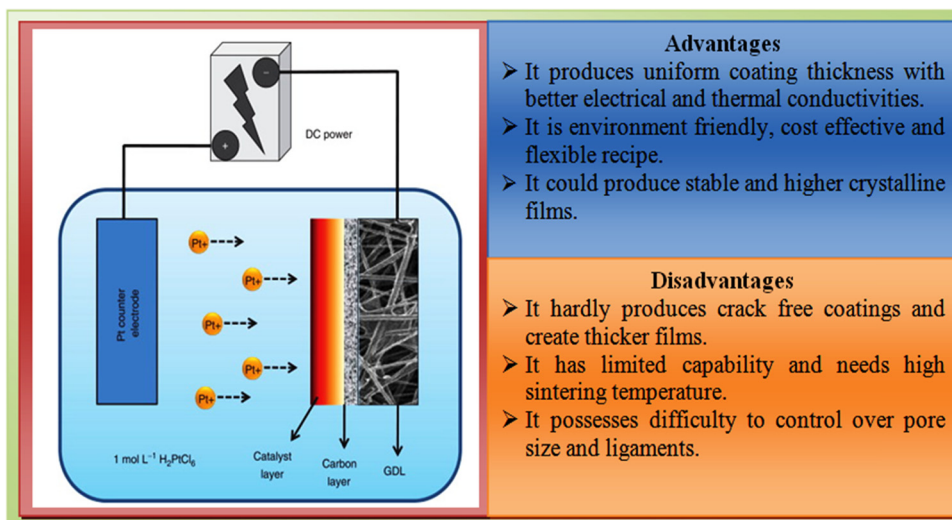


Fig. 11 Overview of the electrodeposition experiment setup together with its advantages and disadvantages.

with direct optical energy band gap of 2.26 eV.<sup>157–162</sup> It is mostly crystallized in a cubic crystalline structure similar to diamond, as shown in Fig. 5,<sup>102,163–171</sup> and a leading material for a wide range of potential applications in solid-state electronic devices such as solar cells, green yellow light-emitting diodes, fluorescent screens, interference filters, laser diodes, solar panel displays, integrated circuits, terahertz radiation detectors, switching devices, gamma-ray detectors, nano-sensors, gas sensors, biomedical imaging devices, electroluminescent devices, electromagnetic field coatings, protective coatings, photodetectors, tandem solar cells, and quantum well structures.<sup>103,172–182</sup>

Considering various applications, the discovery of new materials with advanced physical and chemical properties is highly required, and consequently the properties of materials need to be improved. Thus, to achieve better properties, ZnTe thin films can be doped, annealed, and treated after their deposition on various substrates. The optimization of physical properties such as structural, optical, photoluminescence (PL), electrical, topographical, morphological, and elemental properties of the single layers plays a significant role in device development with better performances. As stated, these properties can be analyzed using different characterization tools such as X-ray diffractometer (XRD), UV-vis spectrophotometer, PL spectrometer, source meter, atomic force microscope (AFM), scanning electron microscope (SEM), and energy dispersive spectroscope (EDS).<sup>183–192</sup> The influence of different

factors on the properties of ZnTe films is discussed in detail herein.

### 3.1 Structural properties

The structural properties of ZnTe thin films are typically investigated using X-ray diffraction (XRD). The evaluation of structural parameters such as crystal structure, inter-planar spacing, internal strain, crystallite size, dislocation density and number of crystallites per unit area of these films can be performed by analyzing their XRD patterns and using the corresponding relations available in the literature.<sup>82,84,102,123</sup> The Scherrer and Williamson Hall relations are well-known approaches for the determination of the crystallite size, while the latter approach can also be used to simultaneously determine the strain as well. ZnTe thin films were deposited using various deposition techniques and it was observed that in most cases, ZnTe thin films were crystallized in the cubic phase with the zinc blende structure having the preferred (111) orientation, as depicted in Tables 2–5 depending on the different growth techniques. Sometimes, ZnTe films are also found to possess a hexagonal phase.<sup>143,189,193</sup>

ZnTe thin films were employed for the development of devices with the architecture of  $\text{ZnO}/\text{CdS}/\text{i-ZnTe}/\text{ZnTe:Cu}/\text{p-GaAs}$  and to explore their viability considering their phase structure, the related research has been carried out thus

Table 5 The film parameters obtained by applying electrodeposition and other techniques

S. no.	Technique	pH/Pa (torr)	$E_g$ (eV)	$D$ (nm)	$\rho$ ( $\Omega$ cm)	Phase	Ref.
1	ED	(3.5 ± 0.1)–(5.5 ± 0.1)	2.26	600	—	Cubic	142
2	ED	—	2.3–1.8	—	—	Cubic	144
3	SILAR	10.1 M	2.75–3.15	75–270	$10^7$ – $10^8$	Cubic	106
4	PLD	$8 \times 10^{-7}$	—	360–790	—	—	194
5	ED	—	—	140	—	Hexagonal	145
6	CSS	$7.5 \times 10^{-6}$	2.16–2.14	17–46	$10^4$ – $10^8$	Cubic	195

Pa: deposition pressure,  $\rho$ : resistivity,  $E_g$ : activation energy, and  $\epsilon$ : relative permittivity.



far. The experimental studies suggest that annealing in an air atmosphere affects phase and structure of ZnTe thin films considerably, which may be owing to the mismatch in the thermal properties of the substrates and developed films and their imperfections including interstitials and vacancies. Accordingly, annealing at a suitable temperature is beneficial to prevent the formation of these imperfections, followed by improving the crystallinity and stoichiometry of the films.<sup>112,143,194</sup> The annealing atmosphere also plays an important role in the modulation of the properties of films. ZnTe thin films were annealed under an argon atmosphere at temperatures of 200 °C, 300 °C, and 400 °C, where randomization in the texture of films occurred, which led to the growth of an additional preferred orientation at 400 °C, revealing to the evaporation of Te from the surface of the films.<sup>113</sup> ZnTe thin films deposited at high substrate temperatures of 280 °C and 300 °C were found to be defect free with high carrier mobility and electrical conductivity<sup>188</sup> but on increasing the substrate temperature further to 400 °C, a slight decrease in crystallinity was observed, which may be due to the re-evaporation of the Te-atoms.<sup>127</sup>

To improve the phase structure of ZnTe films, they have been doped with metals such as copper (Cu), silver (Ag), gadolinium (Gd), and vanadium (V). Copper- and silver-doped ZnTe films were found to be polycrystalline in nature, where their crystallite size decreased for the Ag-doped ZnTe samples and enhanced for the Cu-doped films due to the coalescence of smaller grains.<sup>121</sup> The Cu-doped ZnTe thin films had a higher crystallite size in the range of ~50 nm, as confirmed by Mahmood *et al.*<sup>195</sup> Gd-doped ZnTe thin films have a polycrystalline nature with zinc blende cubic structure but their crystallite size was found to be reduced with an increase in Gd concentration due to the presence of defects involving the substitution of Gd ions and neighboring vacancies.<sup>120</sup> Vanadium (V)-doped ZnTe thin films showed an amorphous nature, where metal doping led to an amorphous nature,<sup>128</sup> while nickel doping did not change the properties of these films greatly.<sup>138</sup> On depositing these thin films with varying angles through the thermal evaporation technique, XRD analysis confirmed that at lower angles, the films were Te rich, at moderate angles with a stoichiometric nature and Zn rich at higher angles.<sup>122</sup> Hence, the structural properties of ZnTe films are affected by several factors, as discussed herein. Together with the phase structure, the optical properties also play great role in film quality and device performance. Thus, the following section is devoted to the optical properties of the ZnTe thin film layers.

### 3.2 Optical properties

The optical properties of ZnTe thin films such as optical absorbance, transmittance, refractive index ( $n$ ), absorption coefficient ( $\epsilon$ ), and energy band gap ( $E_g$ ) are investigated *via* ultraviolet-visible (UV-vis) spectroscopy, which is based on the interaction of light with matter. Their optical properties are typically influenced by the applied growth technique and doping together with pre- and post-treatments. Accordingly, they are affected by annealing, where the absorbance may increase or decrease after annealing the films, which depends on their

crystallinity and grain growth. The interference fringes present in the transmittance spectra confirm the uniform deposition of these films.<sup>112</sup> The pristine ZnTe thin film deposited by the thermal evaporation technique showed a band gap of ~2.20 eV, which was lower than that of its bulk counterpart, which is ~2.26 eV, where a slight reduction was observed for the films annealed at 200 °C be due to the combined effect of annealing inducing a change in the crystallite size and strain in the films.<sup>112</sup> On annealing at 230 °C, they showed a sharp fall in transmittance at the band edge, which verified the good crystallinity of the films with a wide band gap of 2.29 eV.<sup>124</sup> The pristine thin films showed a lower band gap of 1.9 eV compared to the annealed films (2.25 eV) at 350 °C, where excess unbound Te was absent for the annealed films.<sup>196</sup>

The substrate temperature also affects the optical energy band gap of ZnTe thin films. Bacaksiz *et al.*<sup>113</sup> developed ZnTe thin films at substrate temperatures of -123 °C and 27 °C followed by annealing at 200 °C, 300 °C, and 400 °C, where the band gap was elevated to be up to 2.23 eV with annealing and found to be in the vicinity of the standard value of 2.26 eV, while for substrate temperatures of 300 K and 373 K, it was observed at 2.24 eV and 1.95 eV, respectively. The interference patterns in the transmittance spectra confirmed the uniform deposition of these films.<sup>127</sup> As stated, the optical energy band gap of ZnTe thin films is affected by the doped element too, and accordingly undoped ZnTe thin films possessed a band gap of 2.37 eV, while indium doping decreased it to 2.139 eV, which may be due to the change in the acceptor density.<sup>91</sup> Vanadium doping decreased the band gap of ZnTe thin films owing to the decrease in activation energy.<sup>128</sup> The incorporation of oxygen in ZnTe thin films resulted in a variation in band gap, where on increasing the oxygen concentration from 2% to 4%, it increased from 2.2 eV to 3.4 eV, which may be due to formation of oxides in the material.<sup>139</sup> Cu- and Ag-doped ZnTe thin films had a lower transmittance and band gap compared to the undoped films, which was observed due to the formation of defects after doping. The reduction in band gap was attributed to the packing density, which may be due to the increase in crystallite size and decrease in grain boundaries. The band gap of the As-deposited, Cu-doped, and Ag-doped films was found to be 2.23 eV, 2.21 eV, and 2.19 eV, respectively.<sup>121</sup> Similar work was reported for Cu-doped ZnTe thin films, where the transmittance and band gap were found to decrease due to the incorporation of Cu-atoms in the ZnTe lattice.<sup>195</sup>

The optical band gap and transmittance of ZnTe thin films also depend on their thickness, *e.g.*, at a lower thickness of ~564 nm, a higher band gap of 2.265 eV was obtained. Interference fringes were also observed, which indicated the good crystallinity of the deposited films.<sup>197</sup> On depositing ZnTe thin films using the glancing angle deposition technique at different flux angles, the transmittance and band gap were found to increase due to the formation of porous structures as a result of shadowing and quantum confinement effects, respectively.<sup>198</sup> However, when deposition was undertaken using the thermal evaporation technique, a high metallic Zn content was found in the thin films, resulting in a higher



reflectance and lower transmittance.<sup>122</sup> Hence, the optical properties of ZnTe films are greatly modified with pre- and post-deposition treatments. Together with the optical properties, the electrical properties are also correlated with the phase structure, which are affected by several factors, and thus the following section presents a detailed discussion on this.

### 3.3 Electrical properties

The electrical properties of the constituent layers play an important role, where typically for thin films, their conductivity and resistivity can be evaluated using a source meter, which provides current–voltage characteristics. In this case, ZnTe thin films are deposited on ITO, FTO and silicon substrates, where half of them is covered typically by aluminum foil to enable deposition only on half of the substrate, as shown in Fig. 12(a) for ITO substrates. Adhesive silver (Ag) paste is applied to form contacts on both the deposited film and uncoated ITO surface, as shown in Fig. 12(b), where thin copper (Cu) wires with negligible resistance are applied as probes.<sup>181</sup> Besides, Hall measurement and photo-electrochemical cells are also employed to investigate the electrical properties.

As stated, the electrical properties of ZnTe films were studied in terms of conductivity, resistivity, and semiconducting behavior, where these properties are affected by the deposition technique, doping and pre- and post-treatments. The conductivity of these films should be as high as possible for their application in solar cell devices.<sup>143</sup> As stated, Hall measurements are also employed to investigate the electrical properties of ZnTe thin films.<sup>146</sup> Using the electrodeposition technique, ZnTe thin films were deposited at different bath temperatures (30–90 °C), where with an increase in bath temperature, the conductivity was found to increase due to the filling of a separate set of traps lying below the Fermi level.<sup>196</sup> Similarly, p- and n-type semiconducting layers were also prepared *via* the electrodeposition technique, followed by surface treatment employing CdCl<sub>2</sub>. The electrical conductivity obtained by photo-electrochemical cell (PEC) measurements demonstrated increased conductivity for p-type layers.<sup>145</sup> Given that the

conductivity is affected by doping, Mahmood *et al.*<sup>121</sup> showed that ZnTe films with Cu- and Ag-dopant possessed increased conductivity. The Cu-doped films possessed higher conductivity compared to the Ag-doped thin films due to their improved crystal structure with few microstructural defects.<sup>120</sup> The conductivity, carrier mobility, and concentration of ZnTe films were improved with Cu doping.<sup>146</sup> Copper doping in ZnTe films resulted into enhanced charge carrier concentrations, which yielded improved conductivity in the films.<sup>195</sup> The annealing atmosphere and conditions also affect the electrical properties, and accordingly annealing was performed under vacuum conditions and air atmosphere, where annealing in vacuum led to an increase in the conductivity of ZnTe thin films compared to the air-annealed films owing to the changes in their thermal properties by varying the residual gases and different interaction mechanisms with the film surface.<sup>84</sup>

Thus, the electrical properties of ZnTe films are significantly modified with pre- and post-deposition treatments. The surface morphology of the constituent layers of devices also affects film quality and device performance, and therefore, in the next section, we present details on the surface morphology of ZnTe thin films.

### 3.4 Surface morphology

Scanning electron microscopy (SEM) is used to study the surface morphology of ZnTe thin films, where detailed images can be captured by employing field-emission SEM (FESEM). The grain growth, grain size, shape and distribution could also be visualized by analyzing the SEM micrographs. The annealing of these films under different atmospheres, duration and temperature induces and modifies their micro-structural and morphological features. Olusola *et al.*<sup>143</sup> deposited ZnTe films at a cathodic potential of 1600 mV, followed by annealing at 300 °C for 10 min in the air, where the SEM images showed uniformly covered films with varying grain sizes in the range of 127–509 nm due to the agglomeration of small grains.<sup>143</sup> The annealing of ZnTe thin films resulted in a smooth surface with

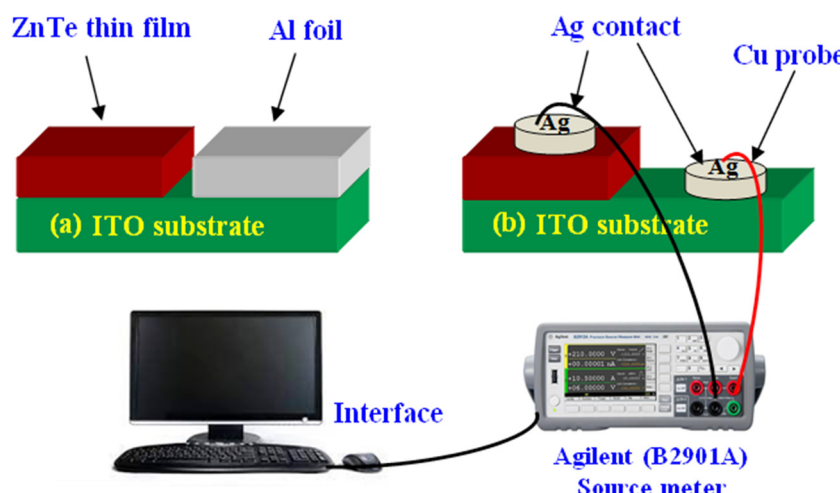


Fig. 12 Illustration of (a) ZnTe thin film deposition on ITO substrate and (b) contact setup for the *I*–*V* measurement along the source meter interface.



reduced intergranular spacing.<sup>196</sup> The substrate temperature also enhanced the grain homogeneity and size due to the increase in the surface diffusion of atoms, which yielded films with voids and domes. The films deposited at substrate temperatures of  $-123\text{ }^{\circ}\text{C}$  and  $27\text{ }^{\circ}\text{C}$  had a grain size in the range of 40–70 nm.<sup>113</sup> The deposition conditions also altered the morphology of the films. The growth time not only led to an altered grain size but also smoother surface.<sup>134</sup> On performing deposition using the GLAD technique, an increase in the deposition angle resulted in an enhanced tilting angle to the nanocolumns of the grown films.<sup>198</sup> As the substrate temperature alters the morphology, ZnTe thin films with triangle-shaped pits were developed on a GaAs substrate with a substrate temperature of  $530\text{ }^{\circ}\text{C}$  using the MBE technique.<sup>133</sup> Cu- and Ag-doped void-free ZnTe thin films with a smoother surface were developed, where the Cu-doped thin films showed a higher grain size compared to that of the Ag-doped and undoped ZnTe thin films.<sup>121</sup> Undoped and Cu-doped ZnTe thin films were developed, where the Cu-doped ZnTe thin films possessed obvious grains and grain boundaries due to the reduction in agglomeration.<sup>195</sup> ZnTe:N thin films were grown at different substrate temperatures using the MBE technique, which consisted of mirror-like compact grains.<sup>132</sup> Findings suggested that doping and annealing significantly enhance the surface morphology of these thin films. Together with the morphology, the elemental composition and stoichiometry of the films also influence their quality and device performance, and thus, in the next section we discuss the compositional properties.

### 3.5 Compositional properties and stoichiometry

The composition of materials can be explored by both elemental dispersive spectroscopy (EDS) and X-ray photoemission spectroscopy (XPS), where EDS is a significant non-destructive X-ray technique and typically used to determine the compositional/elemental properties of powders and films. For the optimum utilization of the source, generally the EDS is coupled with SEM instrumentation, which also makes it cost effective. Considering the target domain, the relevant findings are discussed herein, where a change in composition changes the nature of the films from p- to n-type and *vice versa*. The cathodic potential used during the deposition of ZnTe films influences the weight percentage of Zn and Te elements, and accordingly ZnTe thin films were developed with cathodic potentials of 1500 mV and 1700 mV,<sup>143</sup> where the compositional analysis demonstrated the formation of p-type films with Te richness at a lower cathodic potential and higher cathodic potential resulted in n-type behavior with excess Zn. The thickness evolution showed a decrease in Zn/Te ratio with an increase in ZnTe film thickness.<sup>134</sup> On growing films with positive and negative potential using the electrodeposition technique, the films exhibited richness in Te and Zn elements, respectively.<sup>196</sup> The substrate temperature also affected the weight percentage of Zn and Te elements in these films and the films deposited on glass substrates at different substrate temperatures of  $100\text{ }^{\circ}\text{C}$ ,  $200\text{ }^{\circ}\text{C}$ , and  $400\text{ }^{\circ}\text{C}$  possessed Zn:Te atomic compositions of 54:45, 51:48, and 52:47, respectively, where among them, the findings demonstrated better

stoichiometry of the films deposited at a substrate temperature of  $200\text{ }^{\circ}\text{C}$ .<sup>127</sup> The deposition angle also alters the stoichiometry of the developed constituent layers, and accordingly, ZnTe films were deposited at different angles of  $0^{\circ}$ ,  $20^{\circ}$ ,  $40^{\circ}$ ,  $60^{\circ}$ , and  $80^{\circ}$  employing the thermal evaporation technique, which demonstrated Te richness at lower deposition angles and Zn richness at higher angles. This could be explained based on the kinetic theory of gases or the collisions occurring between the Zn atoms and Te<sub>2</sub> molecules during evaporation.<sup>122</sup> Hence, as deliberated, a number of factors play an important role in controlling the composition and stoichiometry of ZnTe films. The surface topography and roughness also affect the constituent layers of the devices, and thus, in the next section, this is discussed.

### 3.6 Surface topographical properties and roughness

The surface topography of thin films can be evaluated by atomic force microscopy (AFM), which is also known as scanning probe microscopy and generates images of samples with the desired resolution in accordance with the users need and limitations of the instrumentation. AFM analysis provides details on the topography of semiconducting materials at the angstrom scale together with surface roughness and quantitative measurements on grain size, step heights, *etc.* Additionally, advanced AFM measurements enable qualitative mapping regarding various properties and parameters such as adhesion, modulus, dopant distribution, conductivity, surface potential, electric field, and magnetic domains. AFM measurements are undertaken through three modes, *i.e.*, contact, semi-contact and non-contact modes, based on the instrumentation, where equipment is manufactured with one of these modes.

Herein, in accordance with the device architecture or individual constituent layers, the relevant literature available thus far is analysed. The surface roughness of ZnTe thin films was found to decrease with annealing, resulting in the formation of uniform films with enhanced grain size or grain growth, where their 3D images showed columnar growth patterns.<sup>143</sup> Indium doping in ZnTe films resulted into better crystallinity and surface topography.<sup>119</sup> As stated, the substrate temperature affects the surface properties of these films, and accordingly the 3D surface profiles of these films exhibited grainy and polycrystalline topographies, which were fabricated at a substrate temperature of  $100\text{ }^{\circ}\text{C}$  and showed a high domain size with better root mean square of  $\sim 8\text{ nm}$  compared to the films fabricated at other substrate temperatures, *i.e.*,  $27\text{ }^{\circ}\text{C}$ ,  $200\text{ }^{\circ}\text{C}$  and  $400\text{ }^{\circ}\text{C}$ .<sup>127</sup> The topography of the ZnTe films with a thickness in the range of 120–600 nm thickness was revealed to exhibit an increased average roughness from  $6.7\text{ nm}$  to  $33.7\text{ nm}$  and root mean square (RMS) roughness from  $8.27\text{ nm}$  to  $44.2\text{ nm}$ .<sup>124</sup> For MBE grown ZnTe:N thin films, the surface root mean square roughness was found to increase with growth temperature.<sup>132</sup> Hence, surface topographies and statistical parameters of films were greatly influenced by the different pre- and post-treatments as well as the deposition conditions. The individual thin film layers optimized through these tools are employed for the development of devices, and based on the available literature thus far, they are discussed in the followed section together with



the relevant science and importance of the present review domain.

#### 4. Critical insights into the role of ZnTe layers in CdTe thin film solar cells

The research on CdTe thin film solar cells has been predominantly undertaken in the last five decades, where a strong improvement in efficiency has been achieved in the last decade. In 1972, the first CdTe thin film solar cell was introduced by Bonnet and Rabenhorst with a PCE of 6%.<sup>199</sup> Typical CdTe thin film solar cell devices consist of different layered structures, where the superstrate architecture is comprised of glass/TCO/window/absorber/interface/metal contact, as shown in Fig. 13, where a ZnTe layer is employed as an interface.

The transparent conducting oxides (TCOs) are highly degenerative semiconductors, which possess high band gap. Fluorine-doped tin oxide (FTO) and indium-doped tin oxide (ITO) are well known TCO materials, which are employed thus far to develop CdTe devices with the superstrate device structure. To transmit the maximum incident irradiance and develop a heterojunction, a window layer of thickness in the range of 60–100 nm is applied. CdS has a wide band gap of 2.4 eV with n-type nature and is typically used as the window layer in CdTe devices to achieve high efficiency but nowadays magnesium-doped zinc oxide (MZO) has been found to be more transparent and appropriate alternative to the CdS window layer to attain higher power conversion efficiency, together with environmental aspects. To harvest the maximum incident solar irradiance, a CdTe absorber layer having a thickness of 3–5  $\mu\text{m}$  is employed, which has the optical energy band gap of 1.45 eV with p-type conductivity and assures almost complete absorption. The net carrier concentration and lifetime are affected by the crystal structure of the absorber layer, which considerably leads to a change in both the open-circuit voltage ( $V_{\text{oc}}$ ) and short circuit current density ( $J_{\text{sc}}$ ). In recent years, a higher power conversion efficiency has been attained with enhanced  $J_{\text{sc}}$  by introducing

a lower band gap CdSeTe supporting absorber as an interface and replacing CdS with a more transparent and wider band gap material, *i.e.*,  $\text{Mg}_x\text{Zn}_{1-x}\text{O}$  (MZO).<sup>64,66,67</sup> As stated, MZO is a promising alternative to replace the CdS window layer in CdTe-based solar cells and its electron density can be tuned, which provides flexibility in controlling the conduction band offset together with the recombination rates at the TCO/MZO and MZO/Cd(Se)Te interfaces, where the CdTe absorber layer is engineered by employing graded band gap Se (Selenium) insertion to the latter interface.<sup>59,70</sup> The ZnTe semiconducting layer acts as an interface layer between the CdTe absorber and rear-metal contact, which limits the recombination losses dealing with minority carriers due to its captivating performance. To complete the device structure, metal contacts are developed using gold (Au), silver (Ag), copper (Cu) and platinum (Pt) employing the resistive heating-based thermal evaporation technique, but due to high melting point of the Pt leads to radiative heat and its high cost reduce applicability. In the CdTe-based device with a superstrate architecture, this rear metal contact has the task of collecting the charge carriers at the absorber side by contacting the device with an external circuit.<sup>200–207</sup> To date, CdTe solar cell devices with the architecture of glass/MZO/CdSeTe/CdTe/ZnTe/metal contact have demonstrated the maximum power conversion efficiency (PCE) of 22.1%.<sup>32,69,208</sup> CdTe devices with the configuration of glass/FTO/CdS/CdTe/CdCl<sub>2</sub>/ZnTe:Cu/Au demonstrated a PCE of 11.25%, where Cu-doped ZnTe was applied as the back contact. Herein, the CdTe absorber was chloride activated at 360 °C, 380 °C, and 400 °C, where the best performance was attained at 380 °C.<sup>75</sup>

Although the CdTe semiconducting material is a promising absorber material for thin-film solar cell devices, the maximum achieved open circuit voltage ( $V_{\text{oc}}$ ) for these devices is still lower than the theoretically predicated  $V_{\text{oc}}$  due to the barriers developed at the back contact. A simple CdTe device with the configuration of glass/FTO/CdS/CdTe/ZnTe:Cu/Au, as shown in Fig. 14, was developed with copper-doped ZnTe as the back

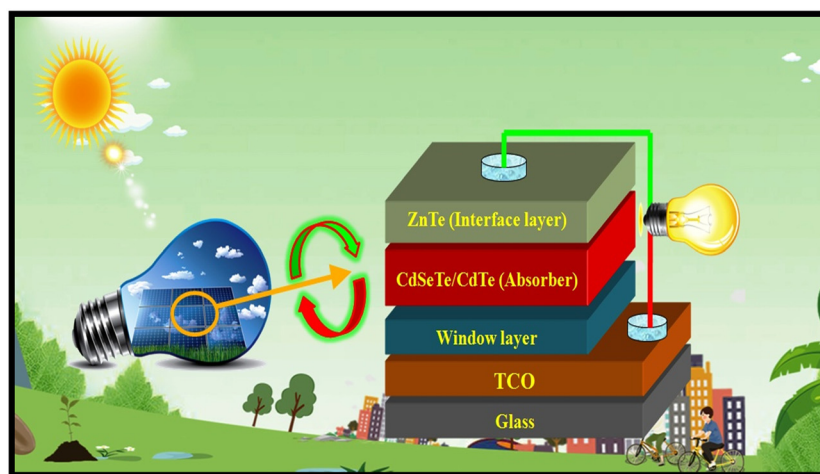


Fig. 13 Pictorial view of ZnTe back contact comprised of CdSeTe/CdTe thin film solar cell device structure together with natural conditions.



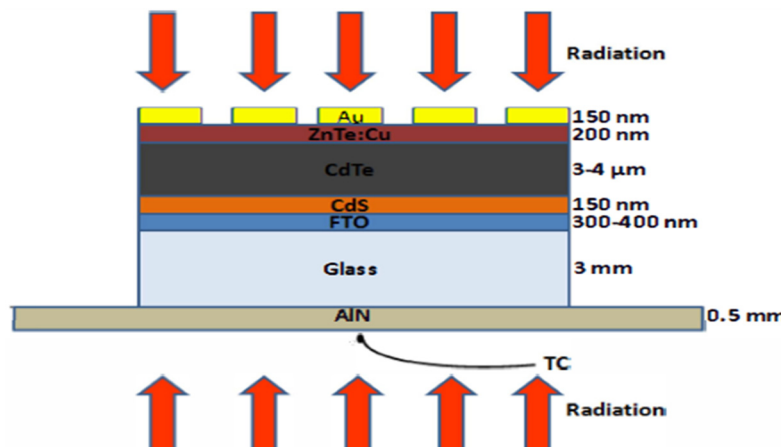


Fig. 14 CdTe solar cell device configuration by employing ZnTe:Cu as the back contact. Reprinted with permission from ref. 209. Copyright (2014) IEEE publications.

contact layer. To control the Cu distribution together with ZnTe:Cu film activation, annealing was performed, where annealing for 30 s at 320 °C improved the fill factor and open circuit voltage, attaining a PCE of 14.5% under the optimal conditions without compromising the short circuit current.<sup>209</sup>

A single-crystal CdTe solar cell device was developed on GaAs substrates by employing metal-organic chemical vapor deposition, where a highly conducting arsenic-doped ZnTe layer was grown on GaAs substrates to act as a buffer layer to the CdTe absorber. The hole concentration in CdTe increased with an increase in VI/II ratio under a high arsenic concentration during the growth mechanism. The electrical findings demonstrated the Ohmic behavior of the CdTe/ZnTe and ZnTe/GaAs contacts. Although the performance in terms of  $V_{oc}$  of 0.63 V and PCE of 4.5% was found to be low, it could be enhanced by decreasing the dislocation density associated with the CdTe thin film layers.<sup>210</sup>

Although persistent efforts have been devoted by researchers thus far to overcome the limitations of the back contact by employing Cu doping, which can form effective back contacts,

the presence of Cu in the CdTe absorber also creates the detrimental recombination centers. In contrast, an effective approach to reduce the back contact barriers in these devices was to introduce a ZnTe:Cu buffer layer with glass/FTO/SnO<sub>2</sub>/CdS/CdTe/(CdCl<sub>2</sub>)/ZnTe:Cu/Au architecture, where both the FF of 73.7% and  $V_{oc}$  of 0.85 V were improved, while the current density of 24.3 mA cm<sup>-2</sup> and PCE of 15.3% remained unchanged, which may be attributed to the passivation of recombination related to defects in the back contact region. The quantitative analysis showed the segregation of the majority of Cu in the Au metallization layer and a ZnTe buffer appeared to inhibit Cu diffusion in CdTe.<sup>211</sup> The relevant energy band diagram is shown in Fig. 15(a and b), where a negligible valence band offset of ~0.1 eV was attained at the CdTe/ZnTe interface but a significant Schottky barrier was present at the ZnTe/Au interface. After Cu doping, the ZnTe:Cu thin film layers became more p-type due to the activation of the Cu dopant, which shifted the valence band offset into a position that reduced barrier to hole transport at the CdTe/ZnTe interface.<sup>211</sup>

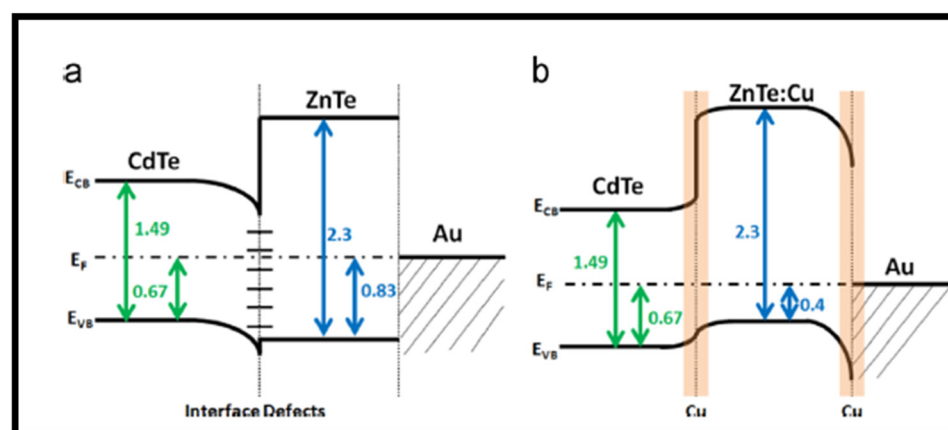


Fig. 15 Energy band diagrams of CdTe devices with (a) undoped and (b) Cu-doped ZnTe back contact. Reprinted with permission from ref. 211. Copyright (2015), Elsevier Publications.



The superstrate architecture devices are finished by the formation of a metal contact on the developed stack of the device, where the metal material also impacts the device performance, and accordingly metal contact material evolution is undertaken with the device configuration of glass/ITO/CdS/CdTe/CdCl<sub>2</sub>/ZnTe/Cu/metal contact where ZnTe is applied as the back contact followed by rf sputtered Cu layer, and then Au, Cr and Ti are applied as metal contacts. The developed devices demonstrated almost similar performances with the maximum PCE of 14.5% for the Au contact.<sup>212</sup> As stated, strong progress in the power conversion efficiency of CdTe solar cells has been recorded for devices with an MZO optical window instead of the conventional CdS by introducing a CdSeTe supporting absorber together with CdTe by modifying the architecture,<sup>64,66,67</sup> causing the highest PCE of 22.1%.<sup>32,69,70</sup> Efforts have also been made to overcome the back contact issues by doping the ZnTe layer with copper to enhance its performance and thickness evolution of ZnTe, where Cu deposited *via* the rf sputtering route at 200 °C substrate temperature with the device structure of glass/FTO/ZnO/CdTe/ZnTe:Cu/Au. The findings demonstrated a PCE of 15.6% for 80 nm ZnTe and 7 nm Cu.<sup>213</sup>

The absorbance in the conventional device architecture of glass/FTO/CdS/CdTe/metal contact at a shorter wavelength is considerably limited by the CdS optical window, where on replacing it by MZO, new insights were revealed. However, the replacement of CdS with magnesium zinc oxide (MZO) resulted in a weak built-in potential at the MZO/CdTe heterojunction and insufficient driving force to repel the photo-generated carriers. Thus, to mitigate this problem, a CdS layer was incorporated between MZO and CdTe based on the architecture of glass/FTO/MZO/CdS/CdSe/CdTe/ZnTe:Cu/Au, and consequently, the built-in potential was improved from 0.369 V to 0.579 V together with an enhanced fill factor, open circuit voltage and quantum efficiency (QE) response.<sup>214</sup> The CdTe device with the structure ITO/ZnO/CdSe/CdTe/ZnTe:Cu/Au is shown in Fig. 16(a) together with the energy band diagram using a 20 nm ZnTe:Cu back contact annealed at 200 °C, and the device yielded a PCE of 6.38%.<sup>215</sup>

Given that a low resistive back contact is needed to fabricate high-efficiency devices, to well match the interfacial properties of ZnTe, a heavily doped p-type Cu<sub>1.4</sub>Te, ZnTe/Cu<sub>1.4</sub>Te alloyed bilayer was synthesized for application in a device with the architecture of glass/FTO/SnO<sub>2</sub>/CdS/CdTe/ZnTe/Cu<sub>1.4</sub>Te/Au, as shown in Fig. 17 with its energy band diagram. This lower Schottky barrier and lesser carrier recombination ZnTe/Cu<sub>1.4</sub>Te-containing device demonstrated a PCE of 15% due to the improved adaption to band bending.<sup>216</sup>

Arsenic-doped ZnTe layers demonstrated higher conductivity compared to the undoped ZnTe, where on applying a heavily doped p-type 100 nm ZnTe:As back contact with the device architecture of glass/ITO/Cd<sub>1-x</sub>Zn<sub>x</sub>S/CdTe-CdCl<sub>2</sub>/ZnTe:As/CdS/CdCl<sub>2</sub>/Au and annealed stack up to ZnTe:As at 420 °C in a hydrogen atmosphere, a significantly enhanced *V*<sub>oc</sub> and PCE 11.9% were achieved.<sup>217</sup> To reduce the back contact barrier, ZnTe:Cu was applied with the device architecture of glass/FTO/SnO<sub>2</sub>/n-CdS/p-CdTe/ZnTe:Cu/Au, and it was revealed that the reaction at the CdTe/ZnTe:Cu interface during the heat treatment process could modify the interfacial band alignment, which reduced the defect-associated recombination and supported the transport of holes, resulting in a PCE of 15.8%.<sup>218</sup> The deposition time and temperature to the ZnTe back contact alter the performance, and accordingly a device was developed with the configuration of glass/FTO/CdS/CdTe/ZnTe/Cu/Au, as depicted in Fig. 18, together with the relevant junction creation mechanism, where ZnTe was deposited at 700 °C for 3 min. The developed device demonstrated a PCE of 12.2%.<sup>219</sup>

A CdTe device with the architecture of glass/FTO/SnO<sub>2</sub>/CdS/CdTe/CdCl<sub>2</sub>/ZnTe:Cu/Mo was developed by employing ZnTe:Cu as the back contact, where a Cu layer was sputtered over ZnTe to improve the charge collection and the devices demonstrated a PCE of 14.3%, which was identical for the 10 nm and 2.5 nm Cu samples annealed at 450 °C and 420 °C, respectively.<sup>220</sup> As stated, the MZO and CdSeTe devices performed better, and accordingly, devices were developed with the architecture of glass/FTO/MZO/CdSeTe/CdTe/ZnTe/Te/C/Ni, as depicted in Fig. 19. The devices developed with a 100 nm ZnTe back contact

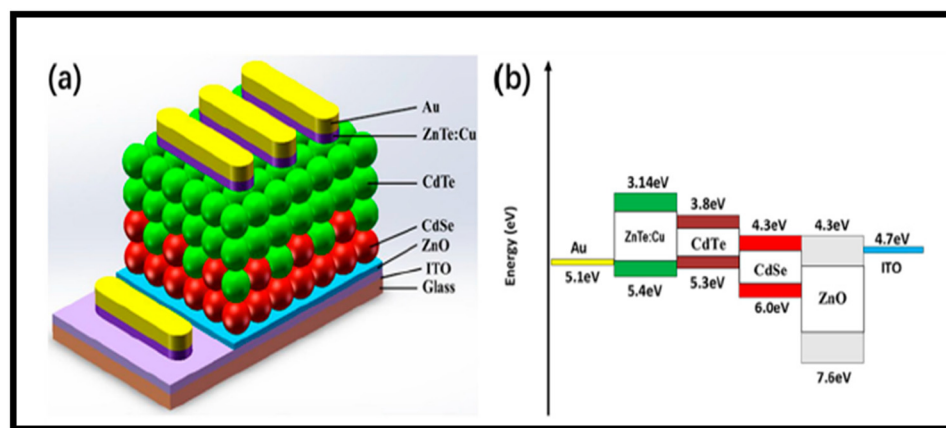


Fig. 16 (a) CdSe and ZnTe:Cu back contact-comprised CdTe device with (b) energy band diagram. Reprinted with permission from ref. 215. Copyright (2019), MDPI Publications.



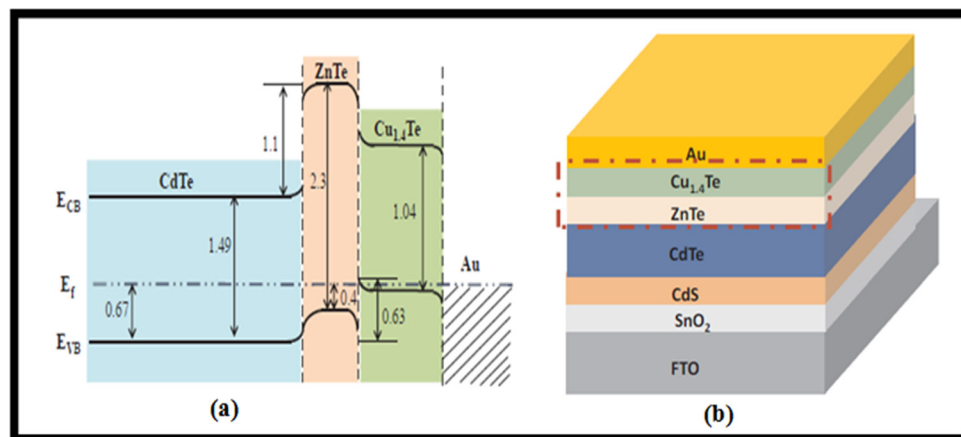


Fig. 17 ZnTe/Cu<sub>1.4</sub>Te-containing glass/FTO/SnO<sub>2</sub>/CdS/CdTe/ZnTe/Cu<sub>1.4</sub>Te/Au architecture CdTe device with (a) energy band diagram and (b) device stack. Reprinted with permission from ref. 216. Copyright (2019), Elsevier Publications.

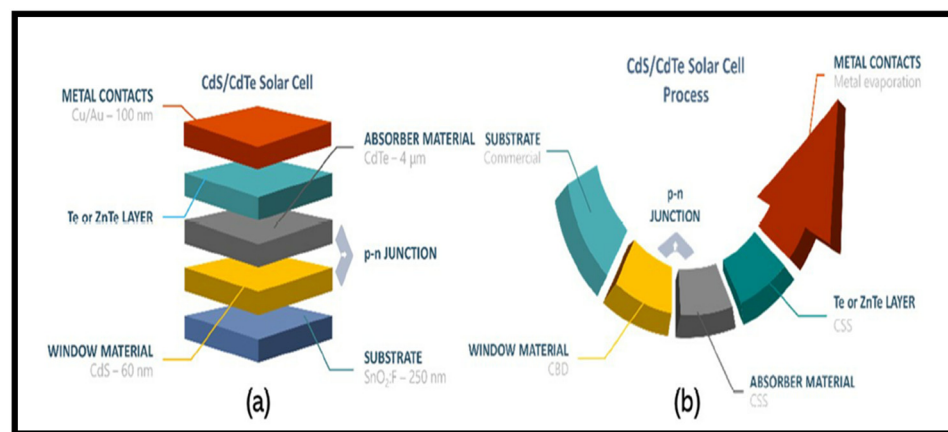


Fig. 18 CdTe solar cell device with architecture of (a) glass/FTO/CdS/CdTe/ZnTe/Cu/Au and (b) pictorial illustration of the junction development mechanism. Reprinted with permission from ref. 219. Copyright (2021), AIP Publications.

annealed at 350 °C for 15 min in an air atmosphere revealed a significant improvement in open circuit voltage, attaining a PCE of 12.96%. In these devices, carbon followed by nickel paint worked as the rear contact, where ZnTe was also followed by a Te layer.<sup>221</sup>

To improve the charge collection in CdTe solar cells in a longer wavelength region, co-evaporated CdSe<sub>x</sub>Te<sub>1-x</sub> layers were employed with the FTO/CdS/CdSeTe/CdTe/ZnTe:Cu/Au structure, where ~3.5 μm CdTe absorber was deposited by close-spaced sublimation with 70 nm 6% Cu-doped ZnTe *via* the thermal evaporation technique, where the optimal band gap of ~1.40 eV of support the CdSeTe absorber resulted in an enhanced PCE of 16.2%.<sup>222</sup> The performance parameters of CdTe devices developed thus far with a ZnTe back contact are presented in Table 6.

An overview of the CdTe solar cell history with the role of the ZnTe back contact is depicted graphically in Fig. 20.

The device design also plays an important role in the development of high-performance devices, and accordingly the following text is devoted to the simulation modeling for designing devices comprised of ZnTe as the back contact layer together with its merits and drawbacks.

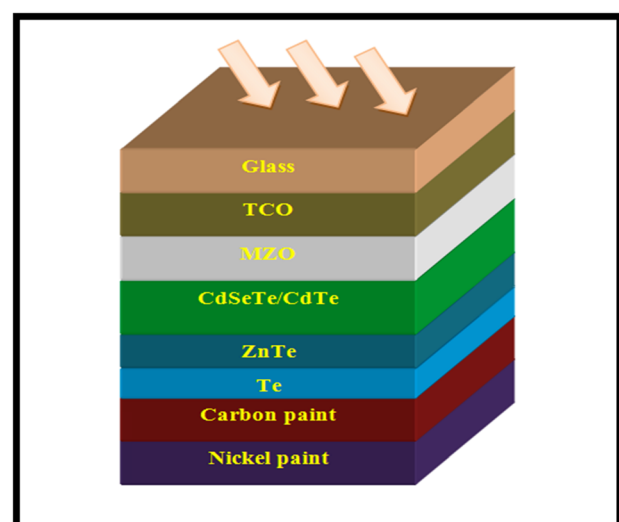


Fig. 19 ZnTe/Te-comprised CdTe device where C/Ni is applied as the rear contact. Reprinted with permission from ref. 221. Copyright (2018), IEEE Publications.

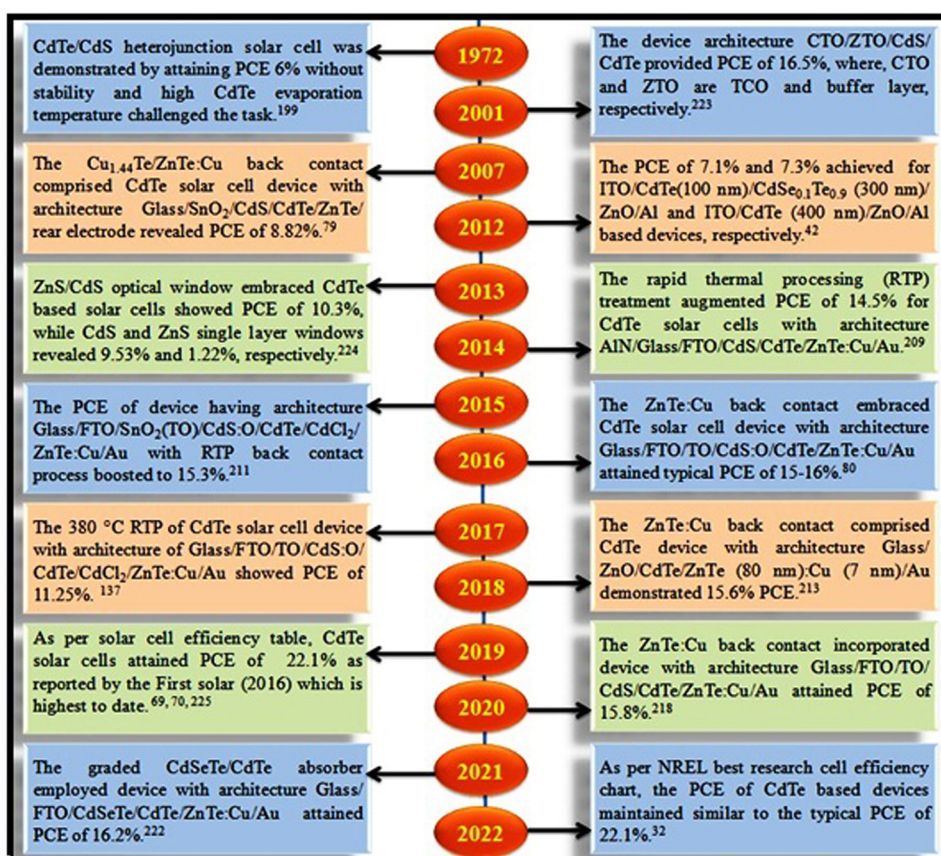
Table 6 An overview of the performance of ZnTe back contact-comprised CdTe devices

Device architecture (s)	$V_{oc}$ (V)	$J_{sc}$ (mA cm $^{-2}$ )	FF (%)	$\eta$ (%)	Ref.
Glass/FTO/CdS/CdTe/CdCl <sub>2</sub> /ZnTe:Cu/Au	0.72	21.99	70.32	11.25	137
Glass/FTO/CdS/CdTe/ZnTe:Cu/Au	0.82	24.3	71.1	14.5	209
CdTe/ZnTe-based device	0.63	16.8	43	4.5	210
Glass/FTO/SnO <sub>2</sub> /CdS/CdTe/CdCl <sub>2</sub> /ZnTe:Cu/Au	0.85	24.3	73.7	15.3	211
Glass/FTO/ZnO/CdTe/ZnTe:Cu/Au	0.83	26.3	71	15.6	213
Glass/ITO/ZnO/CdSe/CdTe/ZnTe:Cu/Au	0.65	19.73	49.75	6.38	215
Glass/FTO/SnO <sub>2</sub> /CdS/CdTe/ZnTe/Cu <sub>1.4</sub> Te/Au	0.81	—	73	15	216
Glass/ITO/Cd <sub>1-x</sub> Zn <sub>x</sub> S/CdTe/CdCl <sub>2</sub> /ZnTe:As/CdS/CdCl <sub>2</sub> /Au	0.69	23.7	72	11.9	217
Glass/FTO/SnO <sub>2</sub> /n-CdS/p-CdTe/ZnTe:Cu/Au	0.83	25.6	74.1	15.8	218
Glass/FTO/CdS/CdTe/ZnTe:Cu/Au	0.74	41.6	39	12.2	219
Glass/FTO/MZO/CdSeTe/CdTe/Te/metal contact	0.77	26.6	62.9	12.96	221
FTO/CdS/CdSeTe/CdTe/ZnTe:Cu/Au	0.82	28.8	68.7	16.2	222
Glass/FTO/MZO/CdSeTe/CdTe/ZnTe/metal contact	0.88	31.7	78.5	22.1	70

A theoretical analysis of CdTe solar cell devices was undertaken using microelectronic and photonic structures to examine their performance parameters, *i.e.*,  $V_{oc}$ ,  $J_{sc}$ , FF, and PCE, where simulations were done by varying the CdTe absorber layer thickness by predicting that a 1  $\mu$ m thick layer was sufficient to get the desired efficiency, and here, the absorber was followed by a 100 nm ZnTe back contact layer to minimize the recombination losses and barrier height, with the device configuration of glass/SnO<sub>2</sub>/Zn<sub>2</sub>SnO<sub>4</sub>/CdS/CdTe/ZnTe/Ni, and a PCE of 22.53% was attained.<sup>226</sup> Although simulation was performed employing

the device architecture of ZnO/CdS/ZnTe/metal-contact, where the ZnTe layer acts as the absorber, CdS as the buffer and ZnO as the optical window employing the solar cell capacitance simulator (SCAPS) code and PCE of 10% attained, the incorporation of grain boundaries is still unclear and the applied absorber is not suitable, and thus simulation still cannot give a clear picture on the optimal device design.<sup>227</sup>

Employing the SCAPS-1D code, a ZnTe:Mo back contact-comprised CdTe device was designed based on the configuration of glass/TCO/ZnO/CdS/CdTe/ZnTe:Mo/metal contact, which

Fig. 20 An overview of the history of ZnTe back contact-comprised CdTe thin film solar cells.<sup>32,42,69,70,79,80,137,199,209,211,213,218,222-225</sup>

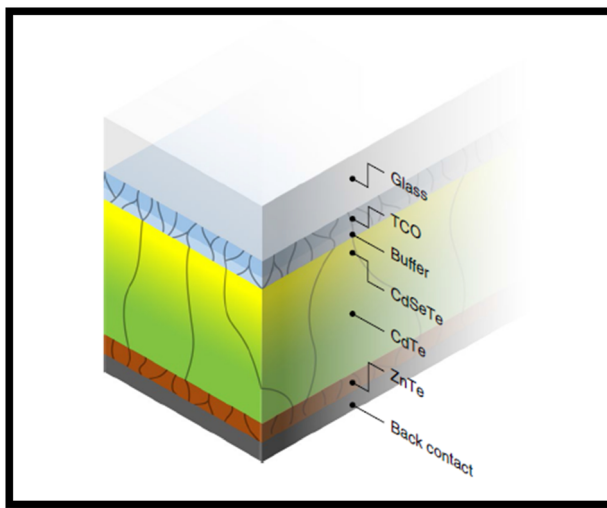


Fig. 21 CdSeTe/CdTe device design with ZnTe back contact employing simulation modeling. Reprinted with permission from ref. 68. Copyright (2019), ACS Publications.

predicted a  $V_{oc}$  of 0.925 V and PCE of 19.06%.<sup>228</sup> Although the SCAPS 1D code has been employed, it does not consider the impact of the grain boundaries in the constituent layers, and therefore the exact mechanism is still unknown, which significantly affects the device performance. The prevalent CdCl<sub>2</sub> treatment and Cu doping of the CdTe absorber were replaced by arsenic (As) to develop a Cu-free back contact, as shown in Fig. 21, with a predicted PCE of 20.8%.<sup>68</sup>

A device was also designed with the architecture of glass/TCO/window layer/CdSeTe/CdTe/ZnTe/back contact, where magnesium-doped zinc oxide (MZO) was employed as the optical window and CdSeTe/CdTe as the absorber layer with the ZnTe interface. The simulation-based photovoltaic parameters of the CdTe device designs having ZnTe back contact layers are presented in Table 7.

As stated, thin film solar cells are comprised of several thin film constituent layers, which contain huge grain boundaries, *i.e.*, two-dimensional defects that act as trap states and recombination centers to the generated and flowed charge carriers. The parallel and perpendicular alignment of these grain boundaries affects the charge carrier flow; however, the simulation codes reported to date do not consider the impact of grain boundaries on the device performance. Thus, the predictions employing simulation codes cannot be applied efficiently in the development of real devices.<sup>39</sup> The power conversion efficiency of single-junction solar cell devices is limited by the Shockley Queisser limit based on the principle of detailed balance, which

could be surpassed by a tandem device, where a narrower absorber band gap sub-cell is stacked by a wider band gap sub-cell to harvest the maximum incident solar irradiance, where light comes from the wider band gap sub-cell side. For tandem devices, the highest recorded PCE 47.1% was reported by NREL, USA for six junction III-V tandems with 143 sun direct incidence AM1.5D,<sup>229</sup> while there is still room for the development of CdTe-based tandems, where the ZnTe back contact embraced CdTe device can be employed as the top sub-cell with perovskite or silicon based bottom sub-cell. The pictorial views of the perovskite/CdTe and c-Si/CdTe tandem architectures are depicted in Fig. 22, which can be employed, but the development of CdTe-based tandem devices is a challenging task for the research community.

## 5. Challenges and opportunities

CdTe thin film solar cells have potential to significantly contribute to meeting the global energy demand by providing a cost-effective road map. Their constituent layers also play a vital role in the optimization of the devices, where in CdTe devices, a ZnTe back contact can reduce the parasitic resistance, while enhancing their performance. In the present review, we concisely discussed the role of the ZnTe back contact in the enhancement of the performances of CdTe thin film solar cells. We also included an overview of the CdTe device development history by incorporating ZnTe back contacts, where the development strategies to produce the ZnTe thin film layers together with the characterization findings thus far were comprehensively discussed including phase structure, optical constants, morphology and topography of the ZnTe single layers to determine their viability in demonstrating better-performance devices. The merits and drawbacks of the development strategies were also presented according to the evolution of materials in terms of doping. The insertion of a ZnTe back contact between the CdTe absorber and metal contact reduces the electron losses by enhancing the open circuit voltage and device performance, which is demonstrated to be important in the modern era of cutting edge energy-driven technology and rivals the evergreen and champion silicon solar cell technology based on a few aspects. Parallel device design work employing simulation modeling has also been reported but still needs experimental validation. The introduction of an MZO optical window and CdSeTe supporting absorber also significantly enhanced the device performance, which opens the applicability of these devices in the tandem architecture as top sub-cells with perovskite and silicon as bottom sub-cells. The simulation modeling codes developed to date do not consider the impact of the grain boundaries on the devices, which is a major roadblock to get device

Table 7 Simulation modeling predictions of ZnTe back contact-containing CdTe devices

Device architecture (s)	$V_{oc}$ (V)	$J_{sc}$ (mA cm <sup>-2</sup> )	FF (%)	$\eta$ (%)	Ref.
Glass/SnO <sub>2</sub> /Zn <sub>2</sub> SnO <sub>4</sub> /CdS/CdTe/ZnTe/Ni	1.06	24.28	87.5	22.53	226
Glass/ZnO/CdS/ZnTe/metal contact	1.81	7.01	78.84	10	227
Glass/TCO/ZnO/CdS/CdTe/ZnTe:Mo/metal contact	0.93	26.87	76.7	19.06	228
Glass/TCO/buffer layer/CdSeTe/CdTe/ZnTe/back contact	0.86	30.5	79.8	20.8	68

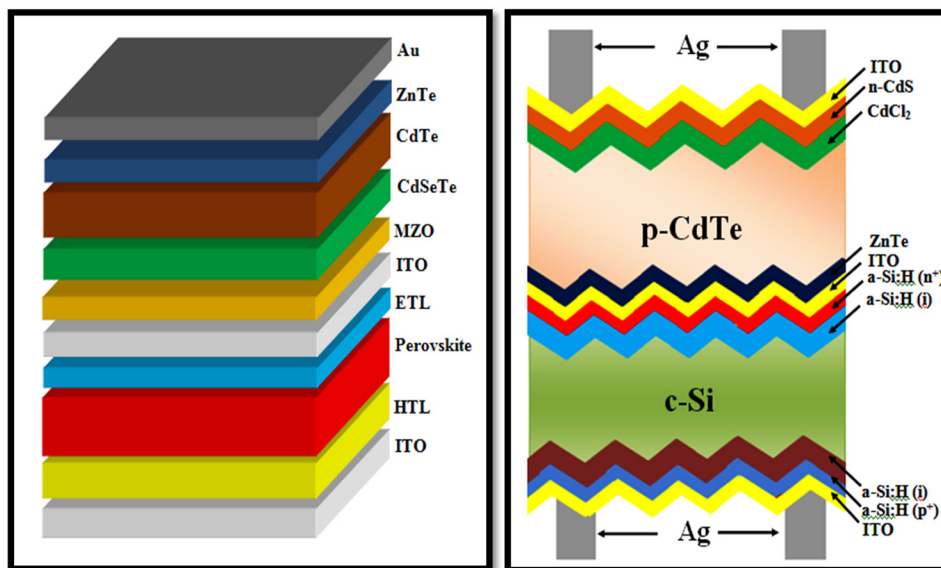


Fig. 22 Graphical illustration of anticipated perovskite/CdTe and Si/CdTe tandem designs, where the CdTe device is suggested as the top sub-cell and perovskite and silicon devices as bottom sub-cells to harvest maximum incident irradiance.

design support in real device development. Considering the findings and obstacles in the development of high-performance devices to cater the present energy needs of society, suitable simulation modeling codes for the design of devices are required comprised of the impact of grain boundaries together with significant work on CdTe-based tandems. Although we attempted to include all the relevant literature dealing with the ZnTe back contact in CdTe devices reported thus far, we apologize if any findings were inadvertently omitted.

## Competing interests

The authors declare that they have no known competing financial interests or personal relationships that could have appeared to influence this review.

## Data availability

All the data presented in the review manuscript are extracted from already published articles as listed in reference section.

## Author contributions

Deepak Suthar: writing – original draft. Sakshi Chuhadiya: writing – original draft. Ritika Sharma: writing – original draft. Himanshu: writing – original draft. M. S. Dhaka: conceptualization, supervision, writing – original draft.

## Conflicts of interest

The authors declared that they have no conflict of interest.

## Acknowledgements

The authors are thankful to Department of Science and Technology, Government of Rajasthan, Jaipur for providing financial support through Research and Development Project Vide file no. F.7(3) ST/R and D/2016/5677 and to the Ministry of Education, Government of India and Ministry of Higher Education, Government of Rajasthan for Research and Innovation project under RUSA 2.0 scheme.

## References

- 1 S. Sinha, D. K. Nandi, S. H. Kim and J. Heo, *Sol. Energy Mater. Sol. Cells*, 2018, **176**, 49–68.
- 2 I. Dincer, *Energy Sources*, 2001, **23**, 83–92.
- 3 I. Dincer, *Sustain. Energy Rev.*, 2000, **4**, 157–175.
- 4 R. Gross, M. Leach and A. Bauen, *Environ. Int.*, 2003, **29**, 105–122.
- 5 A. Harjanne and J. M. Korhonen, *Energy Policy*, 2019, **127**, 330–340.
- 6 M. Shao, Z. Han, J. Sun, C. Xiao, S. Zhang and Y. Zhao, *Renewable Energy*, 2020, **157**, 377–403.
- 7 N. L. Panwar, S. C. Kaushik and S. Kothari, *Renewable Sustainable Energy Rev.*, 2011, **15**, 1513–1524.
- 8 M. K. H. Rabaia, M. A. Abdelkareem, E. T. Sayed, K. Elsaid, K. J. Chae, T. Wilberforce and A. G. Olabi, *Sci. Total Environ.*, 2021, **754**, 141989.
- 9 J. Li, J. Hu and M. Lin, *Renewable Sustainable Energy Rev.*, 2022, **157**, 112084.
- 10 S. Shoeibi, H. Kargarsharifabad, S. A. A. Mirjallily, M. Sadi and A. Arabkoohsar, *J. Energy Storage*, 2022, **50**, 104262.
- 11 N. Kannan and D. Vakeesan, *Renewable Sustainable Energy Rev.*, 2016, **62**, 1092–1105.



12 S. M. Shalaby, S. W. Sharshir, A. E. Kabeel, A. W. Kandeal, H. F. Abosheisha, M. Abdelgaiad, M. H. Hamed and N. Yang, *Energy Convers. Manage.*, 2022, **251**, 114971.

13 V. Devabhaktuni, M. Alam, S. Shekara Sreenadh Reddy Depuru, R. C. Green, D. Nims and C. Near, *Renewable Sustainable Energy Rev.*, 2013, **19**, 555–564.

14 P. A. Owusu and S. A. Sarkodie, *Cogent Eng.*, 2016, **3**, 1–14.

15 V. Kumar, R. L. Shrivastava and S. P. Untawale, *Aquat. Proc.*, 2015, **4**, 473–480.

16 A. H. Ghorashi and A. Rahimi, *Renewable Sustainable Energy Rev.*, 2011, **15**, 729–736.

17 M. Green, E. Dunlop, N. Kopidakis, X. Hao and M. Yoshita, Solar cell efficiency tables (version 57), 2020 pp. 1–13.

18 P. Kittidachachan, T. Markwart, D. M. Bagnall, R. Greef and G. J. Ensell, A detailed study of p–n junction solar cells by means of collection efficiency, *Sol. Energy Mater. Sol. Cells*, 2007, **91**, 160–166.

19 T. I. Mohammed, S. C. L. Koh, I. M. Reaney, A. Acquaye, G. Schileo, K. B. Mustapha and R. Greenough, *Renewable Sustainable Energy Rev.*, 2017, **80**, 1321–1344.

20 P. P. Horley, L. Licea Jiménez, S. A. Pérez García, J. Alvarez Quintana, Y. V. Vorobiev, R. Ramírez Bon, V. P. Makhniy and J. González Hernández, *Thin Film Solar Cells: Modeling, Obtaining and Applications*, 2013, DOI: [10.5772/54058](https://doi.org/10.5772/54058).

21 S. Sharma, K. K. Jain and A. Sharma, *Mater. Sci. Appl.*, 2015, **6**, 1145–1155.

22 A. M. Bagher, M. M. A. Vahid and M. Mohsen, *Am. J. Opt. Photonics*, 2015, **3**, 94–113.

23 M. Askari, V. M. M. Abadi and M. Mirhabibi, *Am. J. Opt. Photonics*, 2015, **3**(5), 275–280.

24 K. L. Chopra, P. D. Paulson and V. Dutta, *Prog. Photovoltaics*, 2004, **12**, 69–92.

25 M. A. Green, Third generation photovoltaics: solar cells for 2020 and beyond, *Phys. E*, 2002, **14**, 65–70.

26 M.-E. Ragoussia and T. Torres, *Chem. Commun.*, 2015, **51**, 3957–3972.

27 N. Kant and P. Singh, *Mater. Today Proc.*, 2022, **56**, 3460–3470.

28 G. K. Rao, K. V. Bangera and G. K. Shivakumar, *Mater. Res. Bull.*, 2010, **45**, 1357–1360.

29 A. A. Bayod-Rújula, *Solar Hydrogen Production Processes, Systems and Technologies*, 2019, pp. 237–295.

30 K. L. Chopra, P. D. Paulson and V. Dutta, *Prog. Photovoltaics*, 2004, **12**, 69–92.

31 C. Becker, D. Amkreutz, T. Sontheimer, V. Preidel, D. Lockau, J. Haschke, L. Jogsches, C. Klimm, J. J. Merkel, P. Plocica, S. Steffens and B. Rech, *Sol. Energy Mater. Sol. Cells*, 2013, **119**, 112–123.

32 <https://www.nrel.gov/pv/assets/pdfs/best-research-cell-efficiencies-rev220630.pdf>, Retrieved August, 2022.

33 S. Sreejith, J. Ajayan, S. Kollem and B. Sivasankari, A Comprehensive Review on Thin Film Amorphous Silicon Solar Cells, *Silicon*, 2022, **14**, 8277–8293.

34 V. M. Fthenakis, *Renewable Sustainable Energy Rev.*, 2004, **8**, 303–334.

35 J. Johansson, *Modeling and Optimization of CIGS Solar Cell Modules*, Master's Thesis, Lund University, Sweden, 2007.

36 K. Sharma, V. Sharma and S. S. Sharma, *Nanoscale Res. Lett.*, 2018, **13**, 381.

37 C. A. Bedolla, R. O. Amaya, J. Hachmann and A. A. Guzik, *Data-driven Discovery for Accelerated Experimentation and Application*, 2013, pp. 423–442.

38 A. J. Nozik, *Phys. E*, 2002, **14**, 115–120.

39 R. Sharma, A. Sharma, S. Agarwal and M. S. Dhaka, *Solar Energy*, 2022, **244**, 516–535.

40 S. K. Sahoo and B. M. N. Sivakumar, *Perovskite Photovoltaics Basic to Advanced Concepts and Implementation*, 2018, pp. 1–24.

41 M. Teena, A. G. Kunjomana, K. Ramesh, R. Venkatesh and N. Naresh, *Solar Energy Mater. Sol. Cells*, 2017, **166**, 190–196.

42 B. I. Mac Donald, A. Martucci, S. Rubanov, S. E. Watkins, P. Mulvaney and J. J. Jasieniak, *ACS Nano*, 2012, **8**, 5995–6104.

43 K. Bewilogua, G. Brauer, A. Dietz, J. Gäßler, G. Goch, B. Karpuschewski and B. Szyszka, *CIRP Annals*, 2009, **58**, 608–627.

44 W. Mahmood, S. U. Awan, A. U. Din, J. Ali, M. F. Nasir, N. Ali, A. U. Haq, M. Kamran, B. Parveen, M. Rafiq and N. A. Shah, *Materials*, 2019, **12**, 1359.

45 H. Singh, T. Singh and J. Sharma, *ISSS J. Micro Smart Syst.*, 2018, **7**, 123–143.

46 S. Lalitha, R. Sathyamoorthy, S. Senthilarasu, A. Subbarayan and K. Natarajan, *Sol. Energy Mater. Sol. Cells*, 2004, **82**, 187–199.

47 R. G. Nair and S. Nampoothiri K, *Int. J. Technol. Res. Eng.*, 2017, **4**, 934–936.

48 A. M. Bagher, M. M. A. Vahid and M. Mohsen, *Am. J. Opt. Photonics*, 2015, **3**, 94–113.

49 K. L. Chopra, P. Paulson and V. Dutta, *Prog. Photovoltaics*, 2004, **12**, 69–92.

50 M. Edoff, *Ambio*, 2012, **41**(Suppl. 2(S2)), 112–118.

51 A. Shah, P. Torres, R. Tscharner, N. Wyrsch and H. Keppner, *Science*, 1999, **285**, 692–698.

52 A. G. Aberle, *Thin Solid Films*, 2009, **517**, 4706–4710.

53 X. He, C. Li, L. Wu, X. Hao, J. Zhang, L. Feng, P. Tang and Z. Du, *RSC Adv.*, 2022, **12**, 22188–22196.

54 K. L. Chopra, P. Paulson and V. Dutta, *Prog. Photovoltaics*, 2004, **12**(23), 69–92.

55 N. R. Paudela and Y. Yan, *Appl. Phys. Lett.*, 2014, **105**, 183510.

56 K. Ohata, J. Saraie and T. Tanaka, *Jpn. J. Appl. Phys., Part 1*, 1973, **12**, 1198.

57 B. E. McCandless, G. M. Hanket, D. G. Jensen and R. W. Birkmire, *J. Vac. Sci. Technol. A*, 2002, **20**, 1462.

58 P. J. Sebastian, *Thin Solid Films*, 1994, **245**, 132.

59 N. Amin, K. Sopin and M. Konagai, *Sol. Energy Mater. Sol. Cells*, 2007, **91**, 1202–1208.

60 D. E. Swanson, J. R. Sites and W. S. Sampath, *Sol. Energy Mater. Sol. Cells*, 2017, **159**, 389–394.

61 T. Ablekim, J. N. Duenow, X. Zheng, H. Moutinho, J. Moseley, C. L. Perkins, S. W. Johnston, P. O. Keefe, E. Colegrave, D. S. Albin, M. O. Reese and W. K. Metzger, *ACS Energy Lett.*, 2020, **5**, 892–896.



62 A. H. Munshi, J. M. Kephart, A. Abbas, T. M. Shimpi, K. L. Barth, J. M. Walls and W. S. Sampath, *Sol. Energy Mater. Sol. Cells*, 2018, **186**, 259–265.

63 T. Ablekim, C. Perkins, X. Zheng, C. Reich, D. Swanson, E. Colegrove, J. N. Duenow, D. Albin, S. Nanayakkara, M. O. Reese, T. Shimpi, W. Sampath and W. K. Metzger, *IEEE J. Photovoltaics*, 2019, **9**(3), 888–892.

64 B. Zhou, X. Yin, J. Zhang, G. Zeng, B. Li, J. Zhang and L. Feng, *Opt. Mater.*, 2020, **110**, 110505.

65 Y. Samoilenco, G. Yeung, A. H. Munshi, A. Abbas, C. L. Reich, M. Walker, M. O. Reese, A. Zakutayev, J. M. Walls, W. S. Sampath and C. A. Wolden, *Sol. Energy Mater. Sol. Cells*, 2020, **210**, 110521.

66 E. Artegiani, A. Gasparotto, P. Punathil, V. Kumar, M. Barbato, M. Meneghini, G. Meneghesso, F. Piccinelli and A. Romeo, *Sol. Energy Mater. Sol. Cells*, 2021, **226**, 111081.

67 A. Munshi, J. Kephart, A. Abbas, J. Raguse, J. Beaudry, J. Sites, J. Walls, K. Barth and W. S. Sampath, *IEEE J. Photovoltaics*, 2018, **8**, 310–314.

68 W. K. Metzger, S. Grover, D. Lu, E. Colegrove, J. Moseley, C. L. Perkins, X. Li, R. Mallick, W. Zhang, R. Malik, J. Kephart, C. S. Jiang, D. Kuciauskas, D. S. Albin, M. M. Al-Jassim, G. Xiong and M. Gloeckler, *Nat. Energy*, 2019, **4**, 1–9.

69 S. Krum and S. Haymore, First Solar Achieves yet Another Cell Conversion Efficiency World record, First Sol, 2016.

70 M. A. Green, E. D. Dunlop, J. H. Ebinger, M. Yoshita, N. Kopidakis and X. Hao, Solar cell efficiency tables (version 56), *Prog. Photovolt. Res. Appl.*, 2020, **28**, 629–638.

71 U. Rau and H. W. Schock, *McEvoy's Handbook of Photovoltaics, Cu(In,Ga)Se<sub>2</sub> Thin-Film Solar Cells*, 3rd Edn, 2018.

72 N. A. Shah and W. Mahmood, *Thin Solid Films*, 2013, **544**, 307–312.

73 K. R. Murali, M. Ziaudeen and N. Jayaprakash, *Solid State Electron.*, 2006, **50**, 1692–1695.

74 J. Li, D. R. Diercks, T. R. Ohno, C. W. Warren, M. C. Lonergan, J. D. Beach and C. A. Wolden, *Solar Energy Mater. Sol. Cells*, 2015, **133**, 208–215.

75 Y. L. Cao, Z. T. Liu, L. M. Chen, Y. B. Tang, L. B. Luo, J. S. Jie, W. J. Zhang, S. T. Lee and C. S. Lee, *Opt. Express*, 2011, **19**, 6100–6108.

76 W. Ni, X. Li, L. Y. Shi and J. Ma, *Nanoscale*, 2022, **14**, 9609–9635.

77 T. W. Kim, H. L. Park and J. Y. Lee, *Appl. Phys. Lett.*, 1995, **67**, 2388.

78 T. W. Kim, D. U. Lee, Y. S. Lim, J. Y. Lee and H. L. Park, *Solid State Commun.*, 1998, **106**, 153–156.

79 L. Feng, L. Wu, Z. Lei, W. Li, Y. Cai, W. Cai, J. Zhang, Q. Luo, B. Li and J. Zheng, *Thin Solid Films*, 2007, **515**, 5792–5797.

80 C. A. Wolden, A. Abbas, J. Li, D. R. Diercks, D. M. Meysing, T. R. Ohno, J. D. Beach, T. M. Barnes and J. M. Walls, *Sol. Energy Mater. Sol. Cells*, 2016, **147**, 203–210.

81 T. A. Gessert, A. R. Mason, P. Sheldon, A. B. Swartzlander, D. Niles and T. J. Coutts, *Vac. Sci. Technol.*, 1996, **14**, 806.

82 D. Suthar, Himanshu, S. L. Patel, S. Chander, M. D. Kannan and M. S. Dhaka, *J. Mater. Sci.: Mater. Electron.*, 2021, **32**, 19070–19082.

83 K. C. Rathod, K. M. Garadkar and P. D. Kambl, *Int. J. Innovative Res. Eng. Sci.*, 2021, **9**, 07–13.

84 D. Suthar, Himanshu, S. L. Patel, S. Chander, M. D. Kannan and M. S. Dhaka, *Solid State Sci.*, 2020, **107**, 106346.

85 B. K. H. AlMaiyaly, B. H. Hussein and A. H. Shaban, *IOP Conf. Ser.: J. Phys.: Conf. Ser.*, 2018, **1003**, 012084.

86 S. Thirumavalavan, K. Mani and S. Sagadevan, *Mater. Today Proc.*, 2016, **3**, 2305–2314.

87 H. Bellakhder, A. Qutzourhit and E. L. Ameziane, *Thin Solid Films*, 2001, **382**, 30–33.

88 G. I. Rusu, M. Diciu, C. Pirghie and E. M. Popa, *Appl. Surf. Sci.*, 2007, **253**, 9500–9505.

89 J. R. Rathod, H. S. Patel, K. D. Patel and V. M. Pathak, *Adv. Mater. Res.*, 2013, **665**, 254–262.

90 A. Pizzo, M. A. Tagliente, L. Caneve and S. Scaglione, *Thin Solid Films*, 2000, **368**, 8–14.

91 P. Link, T. Schmidt, S. Bauer, H. P. Wagner, H. Leiderer and W. Gebhardt, *J. Appl. Phys.*, 1992, **72**, 3730.

92 I. L. Ikhioya, *Int. J. Innovation Appl. Stud.*, 2015, **12**, 369–373.

93 C. W. Huang, H. M. Weng, Y. L. Jiang and H. Y. Ueng, *Thin Solid Films*, 2013, **517**, 3667–3671.

94 C. T. Lee, *Materials*, 2010, **3**, 2218–2259.

95 A. M. Hassan, F. Diab, E. F. Kotp, G. Al-Kashef, E. R. Shaaban and A. E. Metawa, *Opt. Mater.*, 2021, **117**, 111182.

96 S. H. Zyoud, A. H. Zyoud, A. Abdelkader and N. M. Ahmed, *Int. Rev. Model. Simul.*, 2021, **14**, 79–88.

97 I. A. Younus, A. M. Ezzat and M. M. Uonis, *Nanocomposites*, 2020, **6**, 165–172.

98 A. Jilani, M. Shaaban, A. Wahab and A. H. Hammad, *Advance Deposition Techniques for Thin Film and Coating*, 2017. , DOI: [10.5772/65702](https://doi.org/10.5772/65702).

99 Q. Gul, M. Zakria, T. Muhammad Khan, A. Mahmood and A. Iqbal, *Mater. Sci. Semicond. Process.*, 2014, **19**, 17–23.

100 S. H. Mohamed, *J. Phys. D: Appl. Phys.*, 2010, **43**, 1–8.

101 S. L. Patel, Himanshu, S. Chander, A. Purohit, M. D. Kannan and M. S. Dhaka, *Opt. Mater.*, 2019, **89**, 42–47.

102 D. Suthar, Himanshu, S. L. Patel, S. Chander, M. D. Kannan, M. S. Dhaka, D. Suthar, S. L. Patel, S. Chander, M. D. Kannan and M. S. Dhaka, *Int. J. Hydrogen Energy*, 2022, **47**, 14339–14345.

103 R. Sharma, Himanshu, S. L. Patel, S. Chander, M. D. Kannan and M. S. Dhaka, *Phys. Lett. A*, 2020, **384**, 126097.

104 S. Chander and M. S. Dhaka, *J. Mater. Sci.: Mater. Electron.*, 2016, **27**, 11961–11973.

105 S. Antohe, L. Ion, M. Girtan and O. Toma, *Rom. Rep. Phys.*, 2013, **65**, 805–811.

106 S. S. Kale, R. S. Mane, H. M. Pathan, A. V. Shaikh, O.-S. Joo and S. H. Han, *Appl. Surf. Sci.*, 2007, **253**, 4335–4337.



107 A. K. S. Aqili, Z. Ali and A. Maqsood, *Appl. Surf. Sci.*, 2000, **167**, 1–11.

108 B. M. Basol and V. K. Kapur, *Thin Solid Films*, 1988, **165**, 237–241.

109 G. I. Rusu, P. Prepelita, N. Apetroaei and G. Popa, *J. Optoelectron. Adv. Mater.*, 2005, **7**, 829–835.

110 A. A. Ibrahim, *Vacuum*, 2006, **81**, 527–530.

111 A. A. Ibrahim, N. Z. E. Sayed, M. A. Kaid and A. Ashour, *Vacuum*, 2004, **7**, 189.

112 R. Keshav, M. Padiyar, N. M. eghana and M. G. Mahesha, *J. Lumin.*, 2018, **194**, 257–263.

113 E. Bacaksiz, S. Aksu, N. Ozer, M. Tomakin and A. Özçelik, *Appl. Surf. Sci.*, 2009, **256**, 1566–1572.

114 C. H. Hsu, C. F. Tseng, Y. T. Yu, P. C. Yang, C. H. Lai, J. S. Lin and H. W. Yang, *Adv. Mater. Res.*, 2012, **608–609**, 1314–1317.

115 K. Yoshino, A. Memon, M. Yoneta, K. Ohmori, H. Saito and M. Ohishi, *Phys. Status Solidi B*, 2002, **229**, 977–980.

116 G. K. Rao, K. V. Bangera and G. K. Shivakumar, *Vacuum*, 2009, **83**, 1485–1488.

117 E. R. Shaaban, I. Kansal, S. H. Mohamed and J. M. F. Ferreira, *Phys. B*, 2009, **404**, 3571–3576.

118 K. M. U. Rehman, X. Liu, M. Riaz, Y. Yang, S. Feng, M. W. Khan, A. Ahmad, M. Shezad, Z. Wazir, Z. Ali, K. M. Batoo, S. F. Adil, M. Khan and E. H. Raslan, *Phys. B*, 2019, **560**, 204–207.

119 J. Pattar, S. N. Sawant, M. Nagaraja, N. Shashank, K. M. Balakrishna, G. Sanjeev and H. M. Mahesh, *Int. J. Electrochem. Sci.*, 2009, **4**, 369–376.

120 J. D. Lopez, L. Tirado-Mejia, H. Ariza-Calderon, H. Riascos, F. de Anda and E. Mosquera, *Mater. Lett.*, 2020, **268**, 127562.

121 W. Mahmood and N. A. Shah, *Curr. Appl. Phys.*, 2014, **14**, 282–286.

122 T. Hussain, M. F. Al-Kuhali, S. M. A. Durrani and H. A. Qayyum, *Ceram. Int.*, 2018, **44**, 10130–10140.

123 D. Suthar, R. Sharma, A. Sharma, Himanshu, A. Thakur, M. D. Kannan and M. S. Dhaka, *J. Alloys Compd.*, 2022, **918**, 165756.

124 O. Toma and S. Antohe, *Chalcogenide Lett.*, 2014, **11**, 611–618.

125 M. Chakraborty and S. Bhattacharyya, *Vacuum*, 2018, **149**, 156–167.

126 K. N. Raju, R. P. Vijayalakshmi, R. Venugopal, D. R. Reddy and B. K. Reddy, *Mater. Lett.*, 1992, **13**, 336–341.

127 M. Shobana and S. R. Meher, *J. Alloys Compd.*, 2018, **762**, 260–271.

128 M. S. Hossain, R. Islam and K. A. Khan, *Renewable Energy*, 2008, **33**, 642–647.

129 I. S. Yahiaa, A. A. M. Farag, R. Jafer, J. Iqbal, H. Y. Zahran, S. Chusnutdinow, T. Wojtowicz and G. Karczewski, *Mater. Sci. Semicond. Process.*, 2017, **67**, 33–40.

130 Q. Gu, J. Huang, Y. Ma, K. Tang, H. Huang, Y. Hu, T. Zou and L. Wang, *IOP Conf. Ser.: Mater. Sci. Eng.*, 2018, **362**, 012004.

131 S. Jeetendra, C. S. Naveen, P. Raghu and H. M. Mahesh, *Int. J. Eng. Res. Technol.*, 2014, **3**, IJERTV3IS050846.

132 L. Zhang, C. Liu, Q. Yang, L. Cui and Y. Zeng, *Mater. Sci. Semicond. Process.*, 2015, **29**, 351–356.

133 E. Ozceri and E. Tarhan, *Appl. Phys. A*, 2019, **125**, 747.

134 Z. Zhang, J. Li, H. Zhang, X. Pan and E. Xie, *J. Alloys Compd.*, 2013, **549**, 88–91.

135 L. Ouyang, J. Fan, S. Wang, X. Lu, Y.-H. Zhang, X. Liu, J. K. Furdyna and D. J. Smith, *J. Cryst. Growth*, 2011, **330**, 30–34.

136 A. E. Rakhshani, *Thin Solid Films*, 2013, **536**, 88–93.

137 S. Ulicna, P. J. M. Isherwood, P. M. Kaminski, J. M. Walls, J. Li and C. A. Wolden, *Vacuum*, 2017, **139**, 159–163.

138 M. Chaik, S. B. Moumen, R. Bouferra, A. Outzourhit and L. Essaleh, *Superlattices Microstruct.*, 2020, **137**, 1–5.

139 I. Sharma, A. P. Singh, N. Tyagi, N. Saini, S. Auluck and B. R. Mehta, *J. Phys. Chem.*, 2017, **121**, 1488–1497.

140 T. A. Gessert, S. Asher, S. Johnston, M. Young, P. Dippo and C. Corwine, *Thin Solid Films*, 2007, **515**, 6103–6106.

141 T. Mahalingam, V. Dhanasekaran, K. Sundaram, A. Kathalingam and J.-K. Rhee, *Ionics*, 2012, **18**, 299–306.

142 T. Mahalingam, V. S. John, S. Rajendran and P. J. Sebastian, *Semicond. Sci. Technol.*, 2002, **17**, 465–470.

143 O. I. Olusola, M. L. Madugu, N. A. Abdul-Manaf and I. M. Dharmadasa, *Curr. Appl. Phys.*, 2016, **16**, 120–130.

144 M. I. Hossain, Md Kamruzzaman and A. B. M. Obaidul Islam, *J. Mater. Sci.: Mater. Electron.*, 2015, **26**, 1756–1762.

145 O. I. Olusola, M. L. Madugu, O. O. Olusola and S. S. Oluyamo, *Nigeria J. Pure Appl. Phys.*, 2018, **8**, 35–39.

146 D. Kim, K. Park, S. Lee and B. Yoo, *Mater. Chem. Phys.*, 2016, **179**, 10–16.

147 K. P. Acharya, A. Erlacher and B. Ullrich, *Thin Solid Films*, 2007, **515**, 4066–4069.

148 D. A. Gulino, *J. Vac. Sci. Technol.*, A, 1986, **4**, 509.

149 C. X. Shan, X. W. Fan, J. Y. Zhang, Z. Z. Zhang, X. H. Wang, J. G. Ma, Y. M. Lu, Y. C. Liu, D. Z. Shen, X. G. Kong and G. Z. Zhong, *J. Vac. Sci. Technol.*, A, 2002, **20**, 1886.

150 D. Noda, T. Aoki, Y. Nakanishi and Y. Hatanaka, *Vacuum*, 1998, **51**, 619–622.

151 I. A. Younus, A. M. Ezzat and M. M. Uonis, *Nanocomposites*, 2020, **6**, 165–172.

152 M. S. Mohammed, *Eng. Technol.*, 2008, **26**, 1–6.

153 V. Kumar, V. Kumar and D. K. Dwivedi, *Phys. Scr.*, 2012, **86**, 015604.

154 B. Ghosh, D. Ghosh, S. Hussain, R. Bhar and A. K. Pal, *J. Alloys Compd.*, 2012, **541**, 104–110.

155 M. A. Kamran, *J. Sci.: Adv. Mater. Dev.*, 2018, **3**, 226–229.

156 C. Inui, H. Kura, T. Sato, Y. Tsuge, S. Shiratori, H. Ohkita, A. Tagaya and Y. Koike, *J. Mater. Sci.*, 2007, **42**, 8144–8149.

157 M. Chaik, S. B. Moumen, A. Agdad, C. M. SambaVall, H. E. Aakib, H. A. Dads, A. Outzourhit and L. Essaleh, *Phys. B*, 2019, **572**, 76–80.

158 D. C. Sharma, S. Srivastava, Y. K. Vijay and Y. K. Sharma, *Int. J. Recent Res. Rev.*, 2012, **4**, 1–5.

159 T. Potlog, D. Duca and M. Dobromir, *Appl. Surf. Sci.*, 2015, **352**, 33–37.

160 T. Ishizaki, T. Ohtomo and A. Fuwa, *J. Phys. D: Appl. Phys.*, 2004, **37**, 255.

161 Y. Wang, H. Li, T. Yang, Z. Zou, Z. Qi, L. Ma and J. Chen, *Mater. Lett.*, 2019, **238**, 309–312.



162 Y. J. Jang, I. Jeong, J. Lee, J. Lee, M. J. Ko and J. S. Lee, *ACS Nano*, 2016, **10**, 6980–6987.

163 D. C. Sharma, S. Srivastava, Y. K. Vijay and Y. K. Sharma, *Int. J. Res. Rev.*, 2012, **2**, 16–20.

164 F. A. Akgul, G. Akgul, H. H. Güllü, H. E. Unalan and R. Turan, *J. Alloys Compd.*, 2015, **644**, 1–28.

165 R. N. Bhargava, Proceedings of the 17th International Conference on the Physics of Semiconductors, 1985, pp. 1531–1536.

166 A. Romeo and E. Artegiani, *Energies*, 2021, **14**, 1684.

167 A. M. Hassan, F. Diab, E. F. Kotp, G. Al-Kashef, E. R. Shaaban and A. E. Metawa, *Opt. Mater.*, 2021, **117**, 111182.

168 Z. Xiao, Y. Jia, M. Lin, Y. Xia and C. Wang, *ACS Appl. Mater. Interfaces*, 2021, **13**, 8129–8137.

169 C. H. Vasquez, M. A. G. Trujillo, S. G. Hernandez and M. L. A. Aguilera, *AIP Adv.*, 2021, **11**, 035146.

170 J. H. Chang, J. S. Song, K. Godo, T. Yao, M. Y. Shen and T. Goto, *Appl. Phys. Lett.*, 2001, **78**, 566–568.

171 H. Darabian, M. Radha, V. Anjos, M. J. V. Bell, C. Batesttin, A. S. Silva and N. O. Dantas, *J. Non-Cryst. Solids*, 2021, **561**, 120745.

172 N. Pandey, B. Kumar and D. K. Dwivedi, *Adv. Sci., Eng. Med.*, 2020, **12**, 100–104.

173 K. H. Lim, M. T. Man, A. T. Le, J. C. Choi and H. S. Lee, *Thin Solid Films*, 2020, **699**, 137893.

174 J. D. Merchant and M. Cocievera, *J. Electrochem. Soc.*, 1996, **143**, 4054.

175 T. Ota and K. Takahashi, *Solid State Electron.*, 1973, **16**, 1089–1092.

176 S. Zhang, L. Qiu, Y. Zheng, Q. Shi, T. Zhou, V. Sencadas, Y. Xu, S. Zhang, L. Zhang, C. Zhang, C. L. Zhang, S. Hong Yu and Z. Guo, *Adv. Funct. Mater.*, 2021, **31**, 2006425.

177 Z. Wang, T. Wang, C. Zhang, M. Zhang, X. Chen, H. Fan, W. Huang, C. Luan and K. Yu, *J. Phys. Chem. Lett.*, 2021, **12**, 4762–4768.

178 H. Sun, J. Liu, C. Zhou, W. Yang, H. Liu, X. Zhang, Z. Li, B. Zhang, W. Jie and Y. Xu, *ACS Appl. Mater. Interfaces*, 2021, **13**–**14**, 16997–17005.

179 D. Manica, V. A. Antohe, A. Moldovan, R. Pascu, S. Iftimie, L. Ion, M. P. Suche and S. Antohe, *Nanomaterials*, 2021, **11**, 2286.

180 W. Wang, V. Palekis, M. Z. Alom, S. Tawsif Elahi and C. Ferekides, 2021, IEEE 48th Photovoltaic Specialists Conference (PVSC), 2021, pp. 1676–1679.

181 D. Suthar, Himanshu, R. Sharma, G. Chasta, S. L. Patel, S. Chander and M. S. Dhaka, *Phys. E*, 2022, **138**, 115117.

182 V. Palekis, W. Wang, S. T. Elahi, M. Zahangir Alom and C. Ferekides, 2021, IEEE 48th Photovoltaic Specialists Conference (PVSC), 2021, pp. 1293–1297.

183 S. H. Zyoud, A. H. Zyoud, A. Abdelkader and N. M. Ahmed, *Int. Rev. Model. Simul.*, 2021, **14**, 1974–9821.

184 B. K. Ghosh, S. Nasir, K. T. K. Teo and I. Saad, *Mater. Res. Express*, 2021, **8**, 116405.

185 S. Fahad, A. Shuja, B. A. Khan, M. Ali, G. Hassan and S. Alam, *J. Mater. Sci.: Mater. Electron.*, 2021, **32**, 22143–22154.

186 K. Gas, S. Kret, W. Zaleszczyk, E. Kamińska, M. Sawicki, T. Wojtowicz and W. Szuszkievicz, *Materials*, 2021, **14**, 5252.

187 D. Zhai, E. Héroult, F. Garet and J. L. Coutaz, *Opt. Express*, 2021, **29**, 17491–17498.

188 G. K. Rao, K. V. Bangera and G. K. Shivakumar, *Mater. Res. Bull.*, 2010, **45**, 1357–1360.

189 W. Mahmood, S. U. Awan, A. U. Din, J. Ali, M. F. Nasir, N. Ali, A. U. Haq, M. Kamran, B. Parveen, M. Rafiq and N. A. Shah, *Materials*, 2019, **12**, 1359.

190 O. I. Olusola, M. L. Madugu, N. A. Abdul-Manaf and I. Dharmadasa, *Curr. Appl. Phys.*, 2015, **16**, 120–130.

191 S. Rajpal and S. R. Kumar, *Phys. B*, 2018, **534**, 145–149.

192 E. R. Shaaban, L. Kansal, S. H. Mohamed and J. M. F. Ferreira, *Phys. B*, 2009, **404**, 357–362.

193 M. Isik, H. H. Gullu, M. Parlak and N. M. Gasanly, *Phys. B*, 2020, **582**, 1–5.

194 K. S. Lee, G. Oh and E. K. Kim, *J. Korean Phys. Soc.*, 2016, **69**, 416–420.

195 W. Mahmood, A. Thomas, A. U. Haq, N. A. Shah and M. F. Nasir, *J. Phys. D: Appl. Phys.*, 2017, **50**, 255503.

196 T. Mahalingam, V. S. John, S. Rajendra, G. Ravi and P. J. Sebastian, *Surf. Coating Technol.*, 2002, **155**, 245–249.

197 A. M. Salem, T. M. Dahy and Y. A. El-Gendy, *Phys. B*, 2008, **403**, 3027–3033.

198 R. Zarei, M. H. Ehsani and H. R. Dizaji, *Mater. Res. Express*, 2020, **7**, 026419.

199 D. Bonnet and H. Rabenhorst, *Proceedings of the 9th Photovoltaic Specialists Conference*, Silver Spring, MD, USA, 1972, pp. 129–131.

200 K. Kumari, A. Jana, A. Dey, T. Chakrabarti and S. K. Sarkar, *Opt. Mater.*, 2021, **111**, 110574.

201 N. Romeo, A. Bosio and G. Rosa, ISES Solar World Congress 2017.

202 Z. Xiao, Y. Jia, M. Lin, Y. Xia and C. Wang, *ACS Appl. Mater. Interfaces*, 2021, **13**, 8129–8137.

203 T. Potlog, D. Duca and M. Dobromir, *Appl. Surf. Sci.*, 2015, **352**, 33–37.

204 T. Ishizaki, T. Ohtomo and A. Fuwa, *J. Phys. D: Appl. Phys.*, 2004, **37**, 255–260.

205 G. Lastra, P. A. Luque, M. A. Q. Lopez and A. Olivas, *Mater. Lett.*, 2014, **126**, 271–273.

206 A. Barati, A. Klein and W. Jaegermann, *Thin Solid Films*, 2009, **517**, 2149–2152.

207 S. D. Kshirsagar, M. G. Krishna and S. P. Tewari, *Mater. Sci. Semicond. Process.*, 2013, **16**, 1002–1007.

208 M. Green, E. Dunlop, J. Hohl-Ebinger, M. Yoshita, N. Kopidakis and X. Hao, Solar Cell Efficiency Tables (version 59), 2022.

209 J. Li, J. D. Beach and C. A. Wolden, IEEE 40th Photovoltaic Specialist Conference (PVSC), 2014, pp. 2360–2365.

210 P. Y. Su, C. Lee, G. C. Wang, T. M. Lu and I. B. Bhat, *J. Electron. Mater.*, 2014, **43**, 2895–2900.

211 J. Li, D. R. Diercks, T. R. Ohno, C. W. Warren, M. C. Lonergan, J. D. Beach and C. A. Wolden, *Solar Energy Mater. Sol. Cells*, 2015, **133**, 208–215.



212 J. Li, T. R. Ohno and C. A. Wolden, 2016 IEEE 43rd Photovoltaic Specialists Conference (PVSC), IEEE, 2016.

213 A. Bosio, R. Ciprian, A. Lamperti, I. Rago, B. Ressel, G. Rosa, M. Stupar and E. Weschke, *Sol. Energy*, 2018, **176**, 186–193.

214 T. Wang, S. Ren, C. Li, W. Li, C. Liu, J. Zhang, L. Wu, B. Li and G. Zeng, *Solar Energy*, 2018, **164**, 180–186.

215 B. Chen, J. Liu, Z. Cai, A. Xu, X. Liu, Z. Rong, D. Qin, W. Xu, L. Hou and Q. Liang, *Nanomaterials*, 2019, **9**, 626.

216 S. Du, L. Zhu, W. Li, J. Zhang, L. Wu and W. Wang, *Solar Energy*, 2019, **185**, 262–269.

217 O. Oklobia, G. Kartopu and S. J. C. Irvine, *Materials*, 2019, **12**, 3706.

218 K. Shen, X. Wang, Y. Zhang, H. Zhu, Z. Chen, C. Huang and Y. Mai, *Solar Energy*, 2020, **201**, 55–62.

219 C. Hernandez-Vasquez, M. A. González-Trujillo and S. Gallardo-Hernández, *AIP Adv.*, 2021, **11**, 035146.

220 T. Walker, M. E. Stuckelberger, T. Nietzold, N. M. Kumar, C. Ossig, M. Kahnt, F. Wittwer, B. Lai, D. Salomon, E. Colegrove and M. I. Bertoni, *Nano Energy*, 2022, **91**, 106595.

221 A. Kindvall, A. Munshi, T. Shimpi, A. Danielson and W. S. Sampath, IEEE 7th World Conference on Photovoltaic Energy Conversion (WCPEC), 2018, pp. 2994–2997.

222 C. Li, C. Li, Y. Wang, S. Ren, H. Wang, W. Wang, J. Zhang and L. Feng, *Mater. Sci. Semicond. Process.*, 2021, **121**, 105341.

223 X. Wu, R. G. Dhere, D. S. Albin, T. A. Gessert, C. Dehart, J. C. Keane and A. Duda, High efficiency CTO/ZTO/Cds/CdTe polycrystalline thin films solar cells, in: NCPV program review meting, 2001, pp. 14–17.

224 J. Han, G. Fu, V. K. Kumar, C. Liao, W. Jaegermann and M. P. Besland, *J. Phys. Chem. Solids*, 2013, **74**, 1879–1883.

225 M. A. Green, I. Hishikawa, E. D. Dunlop, D. H. Levi, J. Hohl-Ebinger, M. Yoshit and A. W. Ho-Baillie, Solar cell efficiency tables (Version 54), *Prog. Photovolt. Res.*, 2019, **27**, 565–575.

226 M. Deyl, M. Dey, M. A. Matinl and N. Amin, 2015 3rd International Conference on Green Energy and Technology (ICGET), IEEE, 2015.

227 O. Skhouni, A. E. Manouni, B. Mari and H. Ullah, *Eur. Phys. J. Appl. Phys.*, 2016, **74**, 24602.

228 B. K. Ghosh, S. Nasir, K. T. K. Teo and I. Saad, *Mater. Res. Express*, 2021, **8**, 116405.

229 J. F. Geisz, R. M. France, K. L. Schulte, M. A. Steiner, A. G. Norman, H. L. Guthrey, M. R. Young, T. Song and T. Moriarty, *Nat. Energy*, 2020, **5**, 326–335.

